INL/RPT-22-65708-Revision-0

Advanced Reactor Technologies: Gas-Cooled Reactor Fourth Quarter 2021 Report

January 2021

John D Stempien, William E Windes, Michael D McMurtrey, Aaron S Epiney

INL/RPT-22-65708-Revision-0

Advanced Reactor Technologies: Gas-Cooled Reactor Fourth Quarter 2021 Report

John D Stempien, William E Windes, Michael D McMurtrey, Aaron S Epiney

January 2021

Idaho National Laboratory
Idaho Falls, Idaho 83415

http://www.inl.gov

Prepared for the
U.S. Department of Energy
Under DOE Idaho Operations Office
Contract DE-AC07-05ID14517

Page intentionally left blank

INL ART Program

Advanced Reactor Technologies: Gas-Cooled Reactor Fourth Quarter 2021 Report

INL/RPT-22-65708

July, August, and September 2021

Approved by:

Travis Mitchell

Travis R. Mitchell
INL ART Program Manager

3/30/2022
Date

Page intentionally left blank

CONTENTS

FIGURES

TABLES

Page intentionally left blank

ACRONYMS

AGC	Advanced Graphite Creep
AGR	Advanced Gas Reactor
AL	Analytical Laboratory
ASME	American Society of Mechanical Engineers
ASTM	American Society for Testing and Materials
BPVC	Boiler and Pressure Vessel Code
DLBL	deconsolidation-leach-burn-leach
DOE	Department of Energy
DTF	Designed-to-fail
EPRI	Electric Power Research Institute
FACS	Fuel Accident Condition Simulator
FIB	focused ion beam
FIMA	fissions per initial heavy metal atom
FITT	Furnace for Irradiated TRISO Testing
FY	Fiscal Year
GCR	Gas-cooled Reactor
HFEF	Hot Fuel Examination Facility
HTGR	High Temperature Gas Cooled Ractor
HTR	high temperature reactor
HTTF	High Temperature Test Facility
IAEA	International Atomic Energy Agency
IMGA	Irradiated Microsphere Gamma Analyzer
INGSM	International Nuclear Graphite Specialist Meeting
INL	Idaho National Laboratory
IPyC	inner pyrolytic carbon
JAERI	Japanese Atomic Energy Research Institute
LBL	leach-burn-leach
MFC	Materials and Fuels Complex
NEI	Nuclear Energy Institute
NRAD	Neutron Radiography
NRC	Nuclear Regulatory Commission
NSTF	Natural Convection Shutdown Heat-Removal Test Facility
OPyC	outer pyrolytic carbon

ORNL	Oak Ridge National Laboratory
PGS	Precision Gamma Scanning
PICS	Program Information Collection System
PIE	post-irradiation examination
PM HIP	powder metallurgy hot isostatic pressing
POF	probability of failure
PyC	pyrolytic carbon
SB-SMT	single bar simplified model test
SD	standard deviations
SEM	scanning electron microscope
SiC	silicon carbide
SMT	simplified model test
SRF	stress rupture factor
STEM	scanning transmission electron microscopy
TAVA	time averaged, volume averaged
TEM	Transmission electron microscopy
TRISO	tristructural isotropic
UCO	Uranium carbide/oxide
WG	Working group
XCT	X-ray computed tomography

Advanced Reactor Technologies: Gas-Cooled Reactor Fourth Quarter 2021 Report

1 MAJOR ACCOMPLISHMENTS

1.1 Fuels Development

Highlights of Advanced Gas Reactor (AGR) fuels-development activities during July, August, and September 2021 are as follows:

July

- Completed reirradiation of AGR-3/4 Compact 4-3 in the Neutron Radiography (NRAD) reactor at Idaho National Laboratory (INL) and began a 1000°C 300-h test of this compact in the Fuel Accident Condition Simulator (FACS) furnace.
- Completed radial deconsolidation of AGR-3/4 Compact 8-1 at the Analytical Laboratory (AL) at INL after it had been subjected to reirradiation in NRAD and a 1200°C test in the FACS furnace.
- Completed leach-burn-leach (LBL) of the particles and matrix from all segments of radially deconsolidated AGR-3/4 Compact 7-4 and transferred leachates to Oak Ridge National Laboratory (ORNL) Nuclear Analytical Chemistry & Isotopes Laboratory (NACIL). Completed Irradiated Microsphere Gamma Analyzer (IMGA) survey of driver fuel particles from all segments of radially deconsolidated AGR-3/4 Compact 7-4 at ORNL.
- Completed gamma counting with the IMGA of irradiated particles from the 200 h and 400 h, 1400°C oxidation test in the ORNL Furnace for Irradiated TRISO Testing (FITT), which included 10 unirradiated and 10 irradiated AGR-2 Uranium carbide/oxide (UCO) Compact 5-4-2 particles with the outer pyrolytic (OPyC) layer previously removed to expose the silicon carbide (SiC) surface to the oxidizing environment.
- Completed data collection from one particle with an intact buffer layer and one particle with a fractured buffer layer from AGR-2 UCO Compact 5-4-2 using serial sectioning, milling, and imaging in the Scios DualBeam focused ion beam/scanning electron microscope (FIB/SEM).
- Completed a Level 2 milestone at INL to "Transfer AGR-5/6/7 Capsule 1 into the Hot Fuel Examination Facility (HFEF) hot cell and Complete Precision Gamma Scanning (PGS) and Neutron Radiography in NRAD".
- Completed all non-destructive post-irradiation examination (PIE) including visual examinations, neutron radiography at NRAD, and gamma scanning via PGS of the second segment of the AGR-5/6/7 test train comprised of Capsules 3, 4, and 5 at INL.
- Completed a Laboratory Instruction document for the disassembly of the AGR-5/6/7 test train at the HFEF at INL.
- Presented updates from both INL and ORNL staff at the Gas-cooled Reactor (GCR) Program Annual Review.
- Facilitated discussions between INL and ORNL staff and the Technical Coordination Team surrounding the direction of AGR-3/4 PIE related to fission product transport.

August

- Completed radiochemical analyses of LBL solutions from all segments of radially deconsolidated AGR-3/4 Compact 7-4 at ORNL Radioactive Materials AL.

- Completed radial deconsolidation of AGR-3/4 Compact 1-3 at ORNL.
- Completed radial deconsolidation of AGR-3/4 Compact 8-1 at INL. This is the second compact to undergo radial deconsolidation and marks the successful completion of INL Advanced Reactor Technologies (ART) Level 2 Milestone (M2TG-21IN0402048) "Complete Radial Deconsolidation of Two AGR-3/4 Compacts at INL" due September 9, 2021.
- Completed reirradiation of AGR-3/4 Compact 4-3 in the NRAD reactor and completed the 300-h 1000°C test in the FACS furnace at INL.
- Completed NRAD reirradiation and 1400°C FACS testing of AGR-3/4 Compact 1-2 at INL. This supports completion of a Level 2 milestone (M2TG-21IN04020411) that will be submitted in September.
- Completed the INL ART Level 3 Milestone (M3TG-21IN0402043), "Complete Installation and testing of new gamma station in Cell 5 at AL," This milestone was completed on August 24, 2021. The original due date was April 30, 2021, and the revised "expected late" date was September 17, 2021.
- Completed Phase III remote qualifications of the AGR-5/6/7 test train disassembly equipment at the HFEF at INL. Separated Capsules 1 and 2. Opened Capsule 2 and began removing components.

September

- Completed a Level 2 milestone (M2TG-21IN0402047) report, "AGR-2 Tristructural isotropic (TRISO) Fuel PIE Final Report," INL EXT-21-64279.
- Completed two reirradiations and heating tests of AGR-3/4 fuel compacts at Idaho National Laboratory (INL) in fulfillment of a Level 2 milestone (M2TG-21IN04020411).
- Completed Radial deconsolidation of AGR-3/4 Compact 3-1 at INL.
- Opened AGR-5/6/7 Capsule 2 at INL and removed all compacts. Metrology was performed on four compacts from Capsule 2 Level 2, and these were then set aside for PGS.
- Completed Level 2 milestone (M2TG-21IN04020410) to "Complete Phase I qualification of the Air/Moisture Ingress Experiment" at INL.
- Completed SEM of SiC oxidation profiles generated using a FIB to examine select particles from AGR-2 UCO Compact 5-4-2 that were heated for 200 or 400 hours in 21% O2/79% N_2 at 1400°C using the ORNL FITT.
- Completed FITT oxidation test of AGR-2 UCO Compact 5-4-2 particles heated for 400 hours at 1200°C in 21% O_2/79% N_2.
- Submitted Level 3 milestone (M3TG-21IN0402046) report, "Oxidation Testing and Examination of AGR-2 TRISO Particles," ORNL/TM-2021/2092.
- Submitted Level 3 milestone (M3TG-21IN0402045) report, "Radial Deconsolidation and LBL of AGR-3/4 Compacts 8-4 and 7-4," ORNL/TM-2021/2178.

1.2 High-Temperature Materials Development

Highlights of high-temperature materials activities during July, August and September 2021 are as follows:

July

- Completed Level 4 milestone (M4AT-21IN0604021): “Recommendation for Limiting Conditions for American Society of Mechanical Engineers (ASME) Boiler and Pressure Vessel Code (BPVC) Section III Division 5 Allowable Stress Criteria” (INL/EXT-21-63802).
- Attended the July powder metallurgy hot isostatic pressing (PM HIP) process group meeting. This group is a subset of the Section III, Division 1 Task Group Advanced Manufacturing committee.
- Participated in the July American Society of Mechanical Engineers (ASME) Boiler and Pressure Vessel Code (BPVC) Week.
- Completed machining of Alloy 617 compact-tension specimens. The specimens were transferred to undergo a quality inspection. Minor discrepancies between the engineering drawing and the specimens were noted and promptly rectified.
- Finalized the statement of work for a subcontract to leverage a consultant’s industry experience with matching filler metals for Alloy 800H.
- Submitted an IBuy request to set up a subcontract to leverage a consultant’s industry experience with matching filler metals for Alloy 800H.
- Finalized and submitted a report titled “Assessment of Overmatched Filler (Alloy 617) to Improve Alloy 800H Stress Rupture Factors.” This report is the deliverable for milestone M3AT-21IN060405 (INL/EXT-21-63328).
- Participated in the Electric Power Research Institute (EPRI) - Nuclear Energy Institute (NEI) Advanced Reactor Materials Development Workshop.

August

- Attended the August PM HIP process group meeting. This group is a subset of the ASME BPVC Section III, Division 1 Task Group Advanced Manufacturing committee.
- Attended the Gateway for Accelerated Innovation in Nuclear (GAIN) – EPRI - NEI Advanced Methods for Manufacturing Qualification Workshop.
- Submitted Level 4 milestone (M4AT-21IN0604021): “Recommendation for Limiting Conditions for ASME BPVC Section III Division 5 Allowable Stress Criteria” (INL/EXT-21-63802).
- Completed the statement of work for Flatirons Metallurgical Consulting subcontract for technical support.

September

- Completed fiscal year 2022 planning and uploaded to Program Information Collection System (PICS).
- Participated in the Nuclear Regulatory Commission (NRC) Standards Forum.
- Presented on the “Qualification of High Temperature Materials and their incorporation into ASME Section III, Division 5” at the NRC Standards Forum.
- Finished intermediate creep-rupture testing (900°C, 28 MPa) of a small-radius base-metal Bridgeman-notch specimen.

- Set up a subcontract with Materials & Corrosion Know-How B.V. to leverage a consultant's industry experience with matching filler metals for Alloy 800H.
- Set up a subcontract with Flatirons Metallurgical Consulting for technical support.
- Prepared Alloy 800H plates for welding.

1.3 Graphite

Highlights of graphite activities during July, August, and September 2021 are as follows:

July

- Ordered the optics that are needed to upgrade the current Raman spectrometer.
- Completed draft manuscript that summarizes the studies on the thermal diffusivities and microstructure of graphite samples (2114, IG-110, NBG-18, PCEA).
- Commenced draft of manuscript on the microscopic response of thermally annealed nuclear graphite.
- Prepared specimens of IG-110 nuclear graphite to electron transparency via oxidative techniques and thermally annealed and characterized them via transmission electron microscopy (TEM).
- Prepared creep specimens of IG-110 thermally annealed at 2500°C for 81 hrs. and held at a compressive load of 265 lbs. to electron transparency via ion milling.
- Conducted preliminary analysis of creep specimens via TEM.
- Ran a simulation which computed stresses in an oxidized graphite component in order investigate the application of the ASME probability of failure calculation on a degraded graphite component.
- Completed a literature review of irradiation creep models and identified improvements which could be incorporated into the current graphite modeling effort.
- Attended the third 2021 quarterly meeting of the ASME Working Group-General Requirements for Graphite and Ceramic Composite Core Components and Assemblies (WG-GR GCCCCA) and WG-Non-metallic Design and Materials (NDM) held virtually on July 26 and 27, 2021 respectively. Task group feedback included damage tolerance in graphite cores, the development of nuclear graphite specifications, the proposed Weibull and oxidation changes (with submitted ballot records) as well as the development of a graphite component model to support licensing. In addition, a new task group initiative on composite was introduced and the first kick-off is scheduled to take place during the third quarter of 2021. Updates on graphite irradiation data integration as well as molten salt interactions will be provided in the next ASME quarterly meeting.
- Discussed proposal put forth at the ASME NMD WG meeting July 27, to correct some oxidation related statements in ASME BPVC Section III.5 which are either incorrect or not applicable to graphite-moderated AGRs (specifically, high-temperature GCR and Molten Salt Reactors). Based on industry and participant feedback, the proposal will be modified to include short term corrections to Figures HHA-3141-1 and HHA-3141-2, that are currently required for use but are not conservative.
- Opened Ballot 21-2003 for new records #21-728 on HHB composite design corrections and #21-1392 HHA oxidation corrections. The ballot will remain open for four-week period and is set to close on August 12.
- Reviewed Dr. Metcalfe's paper "Damage Tolerance in the Graphite Cores of UK Power Reactors and Implications for New Build" with specific focus to address the code related findings called out during the NRC review. A proposal file was compiled to address these specific code changes.

- Presented status of graphite activities for the past year at the annual Department of Energy (DOE) ART GCR Program Review on July 14, 2021. Graphite activity updates include:
    - Baseline status focusing on Mersen's 2114 and SGL's NBG-17 graphite grades
    - AGC-4 disassembly and PIE status
    - ASME Sec III.5 nonmetallic design and materials working, and task group activities
    - Graphite microstructure characterization activities
    - Behavior model development
    - and Molten Salt – Graphite interaction studies
- Pursued reviews and revisions on a draft of a new paper covering the topic of modeling nuclear graphite oxidation in the kinetic regime. The paper combines experimental oxidation testing (following ASTM 7542), a 3D random pore model, X-ray computed tomography (XCT), and other characterization methods to demonstrate the microstructural and kinetic basis for the large difference in oxidation mass loss between IG-110, PCEA, and NBG-18. The team will continue the internal review process and plan to submit to journal in the near future.
- Continued work on a screening study for uniform oxidation of split disc samples (6 mm by 3 mm, adhering to American Society for Testing and Materials (ASTM) D8289). The planning has included feasibility of XCT to demonstrate uniformity of oxidation as well as simulation of oxidation to compare with experiments. A 6 mm by 3 mm disk of IG-110 was scanned with XCT to determine how uniform the porosity was initially and to build a workflow to measure porosity before and after oxidation.
- Analyzed fractured surfaces of unirradiated and neutron irradiated POCO graphite graded AXF-5Q samples with Raman spectroscopy. The data show an increase on the D peak and a decrease of the G peak at lower irradiation temperatures or/and larger temperature doses. These results are being compared with machined surfaces to assess if the damage created by machining and neutron irradiation are similar. Additional Raman spectra measurements were planned to assess the damage created by the combined effects of machining and neutron irradiation.
- Completed ART Level 3 Milestone (M3TG-21IN05010321), "Complete Oxidation of Irradiated Graphite Status Memo", two weeks in advance of the July 31, 2021, due date.
- Completed ART Level 2 Milestone (M2TG-21IN0501036) "Complete Advanced Graphite Creep (AGC)-4 Disassembly and Issue Report". Report, "AGC-4 Disassembly Report" (INL/EXT-21-63591) was distributed by email (Correspondence Control Number 249901) on July 27, 2021.

August

- Finished construction of UV Raman spectroscopy. Initial testing on IG-110 shows prominent Raman peaks.
- Implemented additional irradiation creep formulation in a graphite model and ran verification simulations.
- Initiated shipping of five AGC-4 samples to INL's Carbon Laboratory. These five samples were separated from the bulk of the AGC-4 samples and sent to the INL AL in July for additional activity measurements.
- Completed initial NRC training on nuclear graphite: Graphite Degradation, Aging, and Failure Mechanisms Sessions 1&2. A third session will be held 20 September 2021.
- Commenced writing technical papers for ASTM Selected Technical Papers (STP)1639 for the Symposium on Graphite Testing for Nuclear Applications: The Validity and Extension of Test Methods for Material Exposed to Operating Reactor Environments.

- Completed ballot review on ASME Boiler & Pressure Vessel Code Subpart HHB corrections for R21-728, and on oxidation changes for R21-1392. Comments are being addressed.
- Held two ASME task meetings to discuss the path forward on how to address graphite damage tolerance as well as in-service inspection methods under Sec XI. One meeting addressed concerns raised by the *NUMARK Report* (ML20344A001) and the *DRAFT REGULATORY GUIDE* (ML21091A276 - DG-1380); the other covered feedback on the changes related to oxidation rules.
- Continued activity on the ASME composite task group effort. The task group aims to address community questions on material qualification processes and its objective is also to work with the community to develop a benchmark study to support the technical basis of the design rules.
- Identified the historic roots of figures HHA-3141-1 and HHA-3141-2 from ASME BPVC Section III Division 5, through analysis of published data on the effect of graphite oxidation on compression strength. HHA-3141-1 is based on compression strength data for uniformly oxidized iso-molded graphite. These data were collected at Brookhaven National Laboratory (1983-1985) and Japanese Atomic Energy Research Institute (JAERI) (1985-1989) and were used by JAERI for the design of High Temperature Test Reactor (HTTR). In contrast, HHA-3141-2 reflects the anomalous behavior of a molded graphite with high content of iron impurities (Brookhaven National Laboratory, 1983).
- Conducted XCT and optical microstructural characterization of uniformly oxidized samples to analyze the effect of shape pore morphology and size in IG-110. The segmentations of the XCT data will be used to estimate the effect of oxidation on some effective properties (elastic modulus, effective thermal conductivity, and permeability) of graphite microstructures.
- Began characterization of neutron irradiated glassy carbon specimens (a prospective material for the protection of nuclear graphite) through Raman spectroscopy, transmission electron microscopy and other characterization techniques to determine the irradiation effects in this material.
- Conducted Raman spectroscopy and x-ray diffraction analysis on neutron irradiated samples of POCO AXF-5Q graphite to understand the irradiation effects in binderless graphite. Raman spectroscopy were conducted on machined, fractured surfaces and polished samples to further understand the effects of surface damage and combined effects with neutron irradiation.
- Confirmed acceptance of abstract *"Recent Reviews, Development and Future Directions in the ASME Section III, Division 5 Code for Graphite and Composite Qualification and Certification"* for a talk at International Nuclear Graphite Specialist Meeting (INGSM)-21.
- Confirmed acceptance of abstract "Recent progress in the microstructural characterization and modeling of nuclear graphite" for presentation at INGSM-21.
- Submitted paper "Multi-scale microstructural analysis of historical and modern nuclear graphite grades" was submitted to the journal *Materials Characterization*.
- Submitted original research paper "Effect of Microstructure and Temperature on Nuclear Graphite Oxidation Using the 3D Random Pore Model" to the journal *Carbon* for peer review.
- Initiated collaboration for a peer-reviewed paper on microstructural changes during high-temperature annealing of nuclear graphite.
- Presented work on defect evolution in high-temperature irradiated nuclear graphite at Boise State University's Micron School of Materials Science and Engineering weekly seminar.
- Completed the INL ART Level 3 Milestone, M3TG-21IN05010327, by issuing the memorandum "Initial Split Disk Testing Results".

- Issued report, “Impact of Flux Wire Selection on Neutron Spectrum Adjustment,” (INL/EXT-21-64191), formally completing the INL ART Level 3 Milestone (M3TG-21IN0501039), “Complete AGC As-Run Uncertainty (Flux Wire Report).”

September

- Initiated the shipment of AGC-4 samples from the HFEF at the Materials and Fuels Complex (MFC) to the Carbon Characterization Laboratory at INL Research Center (IRC).

- Responded to vendor questions on how to initiate graphite certificate holder requests and started the revisions on certificate holder report forms (to be balloted in October through ASME).

- Initiated discussion on review activities related to the composite code detailed under ASME Sec. III Div. 5 Subsect. HH Subpart B, in support of the task group activities.

- Reviewed and integrated the various correspondence from Dr. M. Metcalfe on damage tolerance, functionality, and nuclear safety requirements, into the “Response to NRC questions pertaining to ASME Section III Subsection HH Subpart A, Graphite Materials” (report to be issue by INL). Next action is to initiate discussion to expand the graphite and ceramic composite materials into the ASME code to complete the rules on the non-existing rules on Inservice inspection for graphite and composite components under Section XI.

- Continued consultations between members of ASME Oxidation Task Group on proposed modifications to ASME BPVC Section III Division 5 Subsection HA. Based on analysis of historic strength loss vs. weight loss data, replacement of the 30 % weight loss figure in HHA-3141 (c) with 10 % weight loss has been proposed, which is a more conservative threshold supported by numerous published data. This change will be submitted to Graphite WG before the next ASME meeting.

- Continued analysis of published results on mechanical properties degradation by chronic and acute oxidation of graphite. This analysis will be included in the planned white paper in support of proposed edits to ASME BPVC III 5 HA.

- Completed the framework to estimate the effective properties (thermally conductivity, absolute permeability and elastic modulus) of microstructural based models using XCT.

- Used virtually oxidized XCT reconstructions to estimate the influence of uniform oxidation on the thermal properties, absolute permeability, and elastic modulus of NBG-18 and IG-110.

- Began an effort to upgrade the gas diffusion testing equipment. This includes acquiring new calibration flow controllers and calibrating the experimental flow controller.

- Finished the construction of macroRaman spectroscopy. Noise peaks in the Raman spectrum are analyzed.

- Prepared several graphite samples under different conditions and measured by Raman spectroscopy. The result will be analyzed to study the impact of preparation methods on Raman spectrum.

- Held a preliminary discussion with Erica Belmont (professor at the University of Wyoming) to brainstorm collaboration ideas that could lead to a proposal for DE-FOA-0002516, Consolidated Innovative Nuclear Research , Integrated Research Project, RC-2, Graphite waste management.

- Received two invitations for collaboration on Nuclear Energy University Program proposals and accepted to serve as expert advisor on a pre-proposal sent by U.C. Berkeley.

- Submitted a paper “Effect of Microstructure and Temperature on Nuclear Graphite Oxidation Using the 3D Random Pore Model” to *Carbon*. Comments were received based on three peer reviewers and revisions are being made to resubmit the paper in October.

- Presented at a graphite training seminar to the NRC. This session addressed the modeling work being performed at INL and questions brought up by the NRC at an earlier training session.

- Participated in the virtual ASTM Symposium on Graphite Testing for Nuclear Applications (via Webex), September 23 & 24. One session chair and 3 of the 13 presenters are supported by the ART program.

- Attended the INGSM held virtually via the North Carolina State (Zoom) online platform, September 27-30. Of the 97 registered participants at least 14 are affiliated with ART graphite research.

- Completed ART Level 3 Milestone M3TG-21OR0501054: Publish results of ORNL Irradiation damage and micro structural studies. The publication titled “Probing basal planes and edge sites in polygranular nuclear graphite by gas adsorption: Estimation of active surface area” authored by Nidia C. Gallego, Jose David Arregui-Mena, Cristian I. Contescu, was published in the journal *Carbon*, volume 179, pages 633-645, 2021.

1.4 Methods

Highlights of methods activities during July, August, and September 2021 are as follows:

July

- Conducted and successfully completed by the experimental team, DataQuality070, a low-power two-phase test. This case was performed at baseline test conditions, modified to examine the influence of power at the lowest power levels within the parametric series: 1.4 MW_t in the full scale, or 34.4 kW_t in the Natural Convection Shutdown Heat-Removal Test Facility (NSTF). The facility ran in a transient mode of operation for a period of 25 hours and 13 minutes, during which the test acceptance criteria were successfully met.
- Preparations continued for the planned NSTF shutdown and maintenance period. The facility will be down for approximately four months beginning late August 2021 to repair the faulted Guard heaters, examine the cavity interior, and collect emissivity measurements of the test section and heated surfaces.
- Completed all peer reviews for the DOE Fiscal Year (FY) 21 milestone “RELAP5-3D simulation of PG-27 test at the High Temperature Test Facility (HTTF)”. This has been submitted for final export control review.
- A recurring status meeting (every third Thursday of the month) to coordinate the HTTF benchmark activities has been set-up. The first instance is on August 19th, 2021.
- Progress on the DOE Level 3 (ART-GCR) milestone “Issue paper on Generation of Equilibrium Core Pebble Bed High Temperature Gas Cooled reactor (HTGR) cross sections in a consistent and efficient manner”
    - Developed a 3-D equilibrium core model of the high temperature reactor (HTR)-Pebble Bed Module in Serpent with explicit pebbles and TRISO particles. There are 1,260 different pebbles with distinct isotopic composition fuel and moderator temperatures. The values were obtained from a Griffin equilibrium core calculations with 10 burnup groups and 126 core zones. Six zones were selected at various core locations to prepare microscopic cross sections and neutron spectra for the various pebbles in each zone. We can also prepare data for these zones via infinite domain calculation by using a bounding box and changing the boundary

condition. This enables us to differentiate between local and neighboring effects with a high-resolution model.

    - Continued work on the use of Multiphysics Object Oriented Simulation Environment (MOOSE) stochastics tools to determine the uncertainty in the fuel and moderator temperatures in the same cross section regions as described above. The Griffin equilibrium core solution is loaded into a python script, which runs the stochastic tools for each zone and each pebble type. A Latin hypercube sampler is used to compute the mean and standard deviation in the fuel and moderator temperature in the pebble/TRISO problem for several parameter distributions (power, fluid temperature, heat transfer coefficient, effective local pebble-bed conductivity). The burnup/fluence effects on the various material are also included.
    - Milestone report in the form of a PHYSOR 2022 paper started.

- Progress on the Level 3 (Regulatory Development GCR Methods) Milestone: "Complete report on optimization methodology of pebble bed HTGR start-up and running-in strategy":
    - Developed simplified model of a Pebble Bed Reactor using Serpent for mass transport capability (mflow feature) to simulate pebble movement during burnup
    - Developed a series of tests to verify Serpent new features: 1) mass flow of single and multiple isotopes through simplified geometry model, 2) radioactive decay of representative isotopes in system with flowing mass, 3) reaction rates of isotopes in neutron flux field in system with flowing mass
    - Documentation of methodology that will be part of the milestone report started.

August

- The FY21 milestone (M3AT-21IN0602021) "RELAP5-3D Simulation of PG-27 Test at the HTTF Facility" (INL/EXT-21-63798) has been finalized and formally submitted to DOE.

- The first instance of the recurring status meeting to coordinate the HTTF benchmark activities has been held. Definition of the benchmark problems has been started.

- Two project milestones were completed on schedule and submitted to PICS:NE. The first was an Level 2 milestone deliverable titled "Test Report on Year 3 of Water NSTF Matrix Testing Program" (M2AT-21AN0602012) and provides a summary of FY21 testing on the water-based NSTF covering the two-phase parametric test series. The second was a Level 3 milestone project deliverable titled "Progress Report on Computational Modeling of Water NSTF" (M3AT-21AN0602014) and provides a summary of the computational modeling and analysis performed in FY21.

- DataQuality071, a matrix test within the Loss Coefficient parametric series, was conducted and successfully completed by the experimental team. This case was performed at baseline test conditions with continuous replenishment of boil-off condensate to achieve steady-state mode of flow operation. Restrictions of up to 83% of the nominal flow area were imposed at the inlet to the heated test section, which resulted in initial flow stabilization followed by onset of unstable Type-II density wave oscillations at higher area reductions.

- Preparations continued for the planned NTSF shutdown and maintenance period. The facility will be down for approximately four months starting in early September to repair the faulted Guard heaters, examine the cavity interior, and collect emissivity measurements of the test section and heated surfaces.

September

- The HTTF benchmark will support a PhD student from the University of Tennessee (UTK). The student will move to INL and the INL HTTF benchmark solution will become part of his PhD thesis. A subcontract with UTK has been initiated.
- With the NSTF in cold-shutdown mode for maintenance, disassembly of the heated cavity was completed and repair work started on the two faulted heater Guard zones. In parallel, inspection of the heated cavity is in-progress along with emissivity measurements of the radiation surfaces.

2 SIGNIFICANT ACCOMPLISHMENTS

2.1 Fuels Development and Qualification

2.1.1 Completed AGR-2 PIE

AGR-2 PIE was completed with the writing of a Level 2 milestone report (AGR-2 TRISO Fuel Post-Irradiation Examination Final Report." INL/EXT-21-64279, Idaho National Laboratory). The following are excerpts from the summary and conclusions section of that report.

An array of post-irradiation exams and experiments were employed to assess the irradiation performance and high-temperature behavior of AGR-2 UCO TRISO fuel produced in an engineering-scale coater. Work was also conducted on UO2 TRISO fuel produced for comparison with the AGR UCO fuel. Emphasis was placed on enumerating the frequency of SiC-layer failures (failure of the SiC layer with at least one pyrolytic carbon (PyC) layer remaining intact) and TRISO failures (failure of all three dense layers) and on evaluating the retention of key fission products within the fuel. Examinations of the fuel kernel and coating morphologies were used to understand the features typical of normal, intact fuel, degraded or failed fuel, and mechanisms of degradation. Radiochemical analyses were used to determine fission product retention within the fuel. The results provide a large database on fuel performance and demonstrate that the TRISO failure fractions during normal and accident conditions are significantly lower than those established in historical HTGR design requirements.

2.1.1.1 AGR-2 TRISO Fuel Irradiation Performance

Figure 1 shows the ranges of temperature, burnup, and neutron fluence for AGR-1 and AGR-2 compacts that were subjected to as-irradiated deconsolidation-leach-burn-leach (DLBL) analysis. As-irradiated AGR-1 fuel compacts subjected to similar examinations were irradiated to higher burnups and fluences, while AGR-2 fuel covered higher temperatures and lower burnups and fluences. Between these two experimental campaigns, a broad range of conditions has been explored.

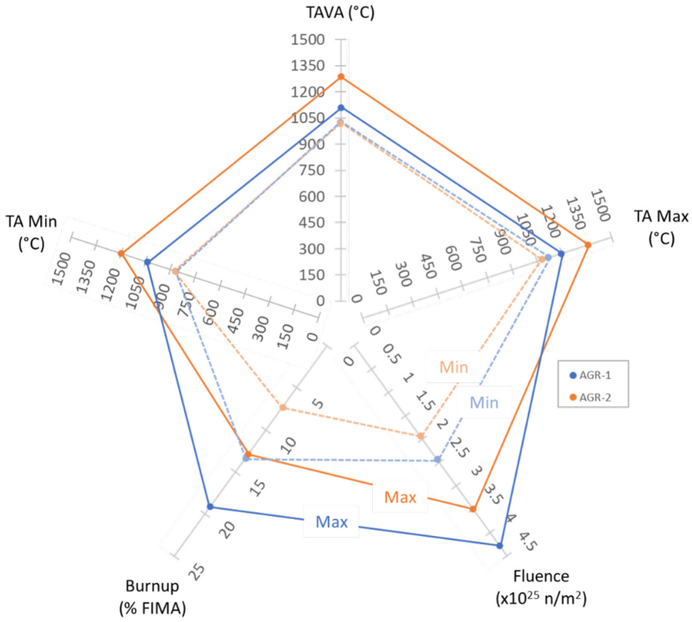

Figure 1. Range of irradiation conditions of AGR-1 and AGR-2 compacts examined in destructive PIE (i.e., DLBL).

2.1.1.2 In-pile SiC and Particle Failure Rates

Online fission gas release data from the early irradiation cycles indicated no particle failures, but operational issues with the test-train gas system beyond the third cycle resulted in the inability to effectively monitor fission gas release. As a result, there were no data available from the irradiation to indicate if any particle failures occurred by the end of the test. Through a combination of PGS scanning of the compact holders to identify compacts suspected of containing exposed kernels and destructive exams of the suspect compacts and particles recovered from these compacts, upper bounds on the number of particles with a TRISO coating that failed during irradiation were determined. The range for the number of failed TRISO particles was 0–4 based solely on PIE data, and the range for failed SiC was 4–10, with the constraint that the number of failed SiC particles plus failed TRISO particles must be ≤10. Therefore, if there were four TRISO failures, there were no more than six SiC failures. Conversely, if there were 10 SiC failures, there were no TRISO failures. Because historical specifications for fuel performance have stipulated limits on acceptable TRISO failure rates but not SiC failure rates, the upper bound on the ranges for failed TRISO particles was used to determine conservative estimates of the actual TRISO failure fractions. Then, binomial statistics were used to determine the upper bound on this failure fraction at 95% confidence. Finally, the constraint on the sum of number of SiC plus TRISO failures gave the number of possible SiC failures, which were also evaluated at 95% confidence.

Table 1 summarizes these upper bounds on the AGR-2 UCO TRISO failure rates and corresponding SiC failure rates. The rates are presented in three groups: Capsule 2 only, Capsules 5 and 6 combined, and all AGR-2 UCO fuel (i.e., Capsules 2, 5, and 6) combined. In all cases, even in the high-temperature Capsule 2 fuel, the as-irradiated UCO TRISO failure rates are significantly better than the historic HTGR design specification of ≤2E-4 at 95% confidence (Stone & Webster Engineering 1986).

While there were no TRISO particle failures identified in the UO_2 fuel based on PIE analyses, it should be noted that the data are not conducive to accurately assessing particle failure fractions because of the relatively low number of total UO_2 particles in the capsule (approximately 18,000). The TRISO failure fraction (upper bound at 95% confidence) for Capsule 3 is ≤1.62E-4.

Table 1. TRISO and SiC failure statistics for as-irradiated AGR-2 UCO fuel.

Capsule	Temperature		Burnup (% FIMA)	Number of Particles	SiC			TRISO		
	TAVA (°C)	TA_{max} (°C)			Number of Failures	Actual Failure Fraction	Failure Fraction Upper Bound [d]	Number of Failures	Actual Failure Fraction	Failure Fraction Upper Bound [d]
2 [a]	1252	1360	12.17	38112	5	1.31E-4	≤2.76E-4	0	0	≤7.87E-5
5 and 6 combined [b]	1088	1197	10.49	76224	1	1.31E-5	≤6.23E-5	≤4	≤5.25E-5	≤1.21E-4
All AGR-2 UCO [c]	1142	1251	11.05	114336	6	5.25E-5	≤1.04E-4	≤4	≤3.50E-5	≤8.01E-5

In cases where the PIE results were inconclusive, the DLBL data were used to define ranges for the possible numbers of SiC and TRISO failures.

a. No TRISO failures were found. Between three and five SiC layer failures were likely, and a conservative value of five SiC layer failures was used.

b. The total number of TRISO failures ranges from zero to four, and a conservative value of four was used. Because the DLBL analysis shows that the sum of the number of SiC failures plus the number of TRISO failures must be five, the conservative choice of assuming four TRISO failures means that one SiC failure is possible. If the true value of TRISO failures is zero, then there would be a total of five SiC failures. The 95% confidence upper limits on the SiC and TRISO failure rates in that case would be 1.38E-4 and 3.94E-5, respectively.

c. In combining all AGR-2 UCO data, the total number of failed SiC particles plus failed TRISO particles is 10. To give this total, the range of failed TRISO particles is from zero to four, and the range of failed SiC particles is from six to 10. The bounding case of four TRISO failures was chosen as a conservative upper limit for this table. If the true value of total TRISO failures in AGR-2 UCO fuel is zero, not four, then at 95% confidence the TRISO failure fraction would be ≤2.63E-5 (not ≤8.01E-5). If the true number of TRISO failures was zero, then there must be 10 SiC failures, not six. At 95% confidence, the overall AGR-2 UCO fuel SiC failure fraction would be ≤1.49E-4 (not ≤1.04E-4).

d. Upper bound at 95% confidence.

2.1.1.3 Particle Morphologies

Thousands of irradiated AGR-2 particles have been observed in metallographic cross sections of loose particles, X-radiography of loose particles, and sectioned fuel compacts. These characterization efforts have led to a wealth of information on fuel behavior during irradiation and during high-temperature, post-irradiation heating tests.

2.1.1.3.1 Kernel Morphology, Volumetric Change, Chemical Evolution

The morphologies of UCO and UO_2 kernels were observed via microscopy. Irradiation-induced volumetric kernel swelling was determined for both UCO and UO_2 AGR-2 kernels and compared to prior work from other programs. UCO kernel swelling ranged from approximately 21 to 30 vol%. This value is comparable to AGR-1 UCO and UCO fuels examined by other programs; however, it occurred at lower burnup, meaning the swelling rate (vol% per % fissions per initial heavy metal atom (FIMA)) in AGR-2 UCO was higher. It is possible that UCO kernel swelling rates may be greater for larger diameter kernels. This would be inverse to the dependency in UO_2 from a previous study that shows faster swelling rates for smaller kernels. The average AGR-2 UO_2 kernel swelling was 10 vol%, with a swelling rate of 0.9 vol% per % FIMA. This is comparable to other studies of UO_2 kernel swelling, but it is noticeably less than the UCO swelling at similar burnups.

The fuel-performance model PARFUME currently uses a fixed kernel volumetric swelling rate of 0.8 vol% per % FIMA for UCO. This value was derived from Light Water Reactor UO_2 fuel. AGR-2 PIE suggests that a higher swelling rate for UCO fuel kernels is appropriate. For UCO kernels similar in size to the 427-µm-diameter AGR-2 kernels, a kernel swelling rate of 2.9 vol% per % FIMA is suggested based on the average of the swelling rates in AGR-2 UCO.

Kernel stoichiometry changed with irradiation. In the unirradiated, as-compacted state the fractions of UO_2, UC_2, UC, and porosity were estimated to be 0.70, 0.205, 0.045, and 0.05, respectively, in AGR-2 UCO kernels. After irradiation, the fuel transformed to a dual-phase structure consisting of UO_2 and UC_xO_y phases. The extent of the UC_2 phases was limited after irradiation. The oxygen in the UC_xO_y phase was in the range of several atomic percent while the UO_2 phase contained extremely low levels of carbon.

2.1.1.3.2 Buffer Morphology and Volumetric Change

It was common to see UCO particles in which the buffer fractured from irradiation-induced dimensional changes. The frequency of buffer fracture in UCO particles varied depending on the irradiation history of the particles (i.e., fluence, burnup, and irradiation temperature). Between zero and 86% of the UCO particles examined from a given compact had buffer fractures. Despite their common occurrence, buffer- inner pyrolytic carbon (IPyC) debonding and buffer fractures generally did not negatively impact TRISO coating integrity or overall fuel performance.

It was found that in AGR-2 UCO fuel particles, buffer fracture frequencies increased with increasing fast fluence and decreasing temperature. The highest buffer fracture frequency occurred at a compact time averaged, volume averaged (TAVA) temperature of about 1100°C and fast fluence of about 3E25 n/m^2. At lower fast fluence and/or higher temperatures, the buffer fracture frequencies were significantly reduced. Lower buffer fracture frequencies were also observed at lower temperatures as long as the fluence was also significantly reduced. These observations are believed to be due to less irradiation-induced dimensional change (shrinkage) of the buffer at lower fast fluence, and higher temperature exposure promoting enhanced creep relaxation of stresses within the buffer, leading to less buffer fracture.

The buffer fracture frequency in AGR-2 UO_2 fuel was significantly less than in UCO fuel irradiated with similar irradiation temperatures and fluences. It could be that the buffers in the smaller-diameter UCO particles saw more fission recoils than the UO_2 buffers surrounding the larger UO_2 kernels. The smaller UCO kernels have a larger surface-area-to-volume ratio, meaning more fission recoils will reach the buffer and induce radiation damage. The reduced amount of kernel swelling measured in the UO_2 fuel relative to UCO could have influenced this behavior, since kernel swelling may drive buffer fracture.

Irradiation-induced shrinkage in the buffer was determined for three UCO compacts and one UO_2 compact. Buffer volumetric shrinkage in the UCO particles ranged from 26 to 29 vol%. Shrinkage in UO_2 buffer was 29 vol%. No fluence dependence was apparent in the shrinkage measurements.

Buffer-IPyC gaps were common in both UCO and UO_2 fuel as the buffer densified and pulled away from the IPyC. The average buffer-IPyC gap thickness was roughly the same for UCO and UO_2 fuel and ranged from 20 μm to 26 μm thick. The gap sizes were similar across the range of fluences available. The buffer may detach from the IPyC by fracturing within itself and leaving buffer tendrils that span the resultant gap, or the buffer may split such that the bulk of the buffer pulls away from the IPyC while a thinner section of buffer remains attached to the IPyC. This kind of morphology was evident in both UCO and UO_2 fuel.

2.1.1.3.3 IPyC, SiC, and OPyC Morphologies

The IPyC was intact in the majority of particles examined, but some IPyC tearing or cracking was observed, typically in the area where the buffer had just started to pull away from the IPyC. Out of 538 particles observed from three different UCO compacts, only 3.5% had IPyC tears, and none of these had through-layer IPyC damage. The extent of IPyC tearing in AGR-2 was less than in AGR-1. This suggests that the bonding strength between the buffer and IPyC in AGR-2 particles may have been lower than in AGR-1 particles. It is hypothesized that this is the result of the longer fluidization time between buffer and IPyC layer deposition during AGR-2 particle fabrication, which made buffer-IPyC separation easier.

The SiC layer was generally intact in the majority of particles examined and showed little or no signs of degradation. In rare, isolated instances, a few particles were found to have damaged SiC layers caused by contamination of transition metals (e.g., Mo) at the time of fabrication or from a thermocouple sheath that failed during irradiation and allowed Ni to migrate and degrade the SiC.

PIE has often identified the presence of a gap at the SiC-OPyC interface in irradiated particles that is not seen in unirradiated particles. This gap is thought to be caused by matrix densification and shrinkage, which pulls the OPyC away from the SiC, or by irradiation-induced shrinkage of the OPyC layer itself. The SiC-OPyC gap was frequently more pronounced in safety-tested samples as identified by both X-radiography and materialographic analyses, and this is presumed to be associated with further shrinkage of the matrix during safety testing. The presence of such a gap means that the OPyC may not always put the SiC layer under compression (as had been assumed in thermomechanical models). The gap does not seem to cause any behavior adverse to fuel performance.

2.1.1.4 Release of Key Fission Products from As-irradiated Fuel

Because failed SiC layers were exceedingly rare (occurring at a rate of 5.25E-5 in AGR-2 UCO fuel during irradiation), little fission product ^{134}Cs was measured outside of fuel compacts. A fraction of about 4E-5 was measured outside of the UCO fuel compacts in Capsules 5 and 6. This is commensurate with the estimated as-fabricated exposed kernel fraction of ≤4E-5 in the UCO fuel. In UCO Capsule 2, which was an average of about 150°C hotter than UCO Capsules 5 and 6 and about 220°C hotter than UO_2 Capsule 3, a fraction of about 9E-5 of the ^{134}Cs was released from the compacts. Only a fraction of 2E-6 was released from UO_2 Capsule 3 compacts. This is less than the estimated as-fabricated exposed kernel fraction in UO_2 fuel, but about twice the dispersed uranium fraction in UO_2 compacts, indicating extremely small release through intact TRISO coatings. In all cases, the fuel exhibited good retention of ^{134}Cs, but the cooler UO_2 fuel appeared to have retained a little more ^{134}Cs than the UCO fuel.

Fission gases (e.g., Kr and Xe) were not found in the TRISO coatings, but they were observed in the kernels using microscopy-based elemental analyses. In UCO fuel, Kr and Xe preferentially occupied the UC_xO_y phases in preference to the UO_2 phase. Iodine is a volatile fission product that was generally seen in the same regions of the particle as Xe and Kr. This observation may be caused in part by the radioactive decay of some iodine isotopes to stable isotopes of Xe.

Silver is known to diffuse through intact TRISO coatings, and this release is highly temperature dependent. Based on ^{110m}Ag measured outside of the fuel compacts and from comparing measured compact inventories to their predicted ^{110m}Ag inventories, ^{110m}Ag release dramatically increased with temperature in the range of 1000 to 1100°C. From about 1125 to 1300°C, ^{110m}Ag release from compacts averaged about 80%, but it could be as low as about 65% or as high as about 99%. This is consistent with a rapid increase in the silver diffusion rate through intact SiC layers at temperatures ranging from approximately 1100 to 1300°C observed in multiple post-irradiation heating tests. Indications were that UO_2 fuel retains Ag marginally better than UCO fuel at the same irradiation temperature. When Ag was observed via microscopy in a UCO kernel, its concentration tended to be higher at the kernel-buffer interface than at the center of the kernel. Any silver that diffuses beyond the SiC layer is not well retained by the compact matrix, and the vast majority of Ag that diffuses through intact SiC layers will be released from the compact altogether.

Radioisotopes of palladium are not readily detectable by gamma or beta spectroscopy, and the complicated makeup of the samples makes quantification of Pd by mass-spectrometry extremely difficult. Palladium is of interest, however, because it has been observed to react chemically with the SiC layer in UCO particles. Energy-dispersive spectroscopy maps showed that Pd was more enriched in the UO_2 phase than in the predominantly carbide phases of the UCO kernels. Furthermore, Pd concentrations tended to be higher at the kernel-buffer interface than at the center of the kernel.

Palladium has been observed across the IPyC and SiC layers. The Pd concentration increased across the IPyC and was found to be highest on the SiC side of the IPyC-SiC interface in UCO fuel. From there, the Pd concentration decreased farther out in the SiC layer. Overall, Pd-SiC interactions do not challenge the performance margin of UCO fuel.

Some Eu was released through intact coatings in all of the capsules, but the release was much more pronounced in the hottest AGR-2 capsule, UCO Capsule 2 (TAVA temperature of 1252°C). A little less than 4% of the Capsule 2 inventory of Eu was released from the compacts. Roughly 1000 times less Eu was released from the 150°C-cooler Capsule 5 UCO fuel. No Eu was detected outside of the compacts in UO_2 Capsules 3 (TAVA temperature of 1032°C) or UCO Capsule 6 (TAVA temperature of 1074°C). Strontium is typically observed to behave in ways similar to Eu. About 1% of the Capsule 2 inventory of Sr was released from its UCO fuel compacts. Capsules 5 and 6 UCO compacts released Sr in fractions of 6E-5 and 8E-5. The UO_2 fuel compacts in Capsule 3 released a fraction of 1.3E-4, more Sr than was released from the UCO fuel compacts in Capsule 5 and 6. This indicates that UCO fuel better retains Sr than UO_2 at similar temperatures.

Over the range of AGR-2 irradiation temperatures, the Sr and Eu release rates from UCO compacts appear to increase more noticeably between average irradiation temperatures of 1100 and 1250°C. At these higher temperatures, Eu and Sr were still largely retained by the kernel, but their highest concentrations were observed at the periphery of the kernel. At lower irradiation temperatures, Eu and Sr concentrations were highest in the center of the kernel. Unlike Ag, which is not well retained in the OPyC and compact matrix outside of particle SiC layers, substantial Eu and Sr is retained in the compact matrix.

2.1.1.5 High-Temperature Safety-Test Performance

A total of 18 AGR-2 fuel compacts (14 UCO compacts and four UO_2 compacts) were subjected to post-irradiation safety tests ranging from 1500 to 1800°C in the Core Conduction Cooldown Test Facility at ORNL. Tests featured isothermal holds at the designated temperature for nominally 300 h. One test of three UCO compacts used a time-varying temperature program that simulated an HTGR temperature transient with a peak temperature of 1695°C. Releases of key radionuclides (i.e., ^{85}Kr, ^{90}Sr, ^{110m}Ag, ^{134}Cs, and ^{154}Eu) from safety-tested AGR-2 UCO fuel compacts were similar to those of AGR-1 UCO fuel.

2.1.1.5.1 Safety-Test Particle and SiC Failure Rates

Isothermal post-irradiation safety tests of AGR-2 UCO fuel were conducted for six compacts at 1600°C and five compacts at 1800°C. These temperatures were maintained for 300 hours in each test. The time-dependent releases of key fission products (e.g., ^{85}Kr and ^{134}Cs) were measured, and post-safety test destructive exams of the fuel compacts were used to identify the number of particles degraded by the elevated-temperature exposure and the causes of that degradation.

Table 2 summarizes the SiC and TRISO measured failure fractions and upper bounds on the failure fractions at 95% confidence from safety tests of AGR-2 UCO compacts. The overall SiC and TRISO failure rates from the AGR-2 UCO fuel irradiation (summarized in Section 2.1.1.2) are included in the top row of Table 2 for comparison. The safety-test failure rates are presented in three groups: Capsule 2 only, Capsules 5 and 6 combined, and all AGR-2 UCO fuel (i.e., Capsules 2, 5, and 6) combined. Historic reactor design specifications established that the TRISO failure fraction be limited to ≤6E-4 (at 95% confidence) during reactor accidents with peak fuel temperatures of 1600°C (Stone & Webster Engineering 1986). There were no SiC or TRISO failures from 1600°C testing in AGR-2. In all cases, even in the high-temperature AGR-2 Capsule 2 fuel, the AGR-2 UCO TRISO failure rates from 1600°C safety tests were significantly better than the historic HTGR design specification. These calculated failure rates could be lower if the sample size were increased through additional testing.

One safety-test-related failure of a UCO TRISO particle occurred during the 1800°C safety test of AGR-2 UCO Compact 2-3-2. This failure was traced to particle attack by Mo contamination that originated from particle fabrication that could be avoided using a different approach for removing particles samples during coater operation; therefore, it is not counted as a particle that failed from inherent fuel-performance phenomena. It was determined that either zero or one TRISO particle failed in the 1800°C test of Compact 6-2-1. The values in Table 2 were calculated assuming one TRISO failure in Compact 6-2-1. The note below the table gives the TRISO failure rates (upper bound at 95% confidence) if there was no TRISO failure in Compact 6-2-1. There are no historic reactor design specifications for TRISO performance at 1800°C (historic HTGR designs prevented fuel from reaching that temperature); however, the conservative AGR-2 UCO TRISO failure rates from 1800°C safety tests are significantly better than the historic HTGR design specification for 1600°C performance. It is possible that these rates would be even lower if the sample size was increased.

The referenced reactor design specifications for particle failure during accidents involve a peak core temperature of 1600°C (the design-limited peak core temperature for a depressurized loss-of-forced cooling accident), but the average core temperature will be much lower. In addition, the peak temperature during the accident is attained for a relatively short duration (several hours), whereas the isothermal safety tests presented in this report held all the particles at the test temperature for ~300 hours. These tests are not intended to directly mimic an HTGR accident, but rather bound the accident conditions, as they are in fact much more severe for the fuel particles in terms of the time-at-temperature compared to the fuel in an HTGR core during a depressurized loss-of-forced cooling accident.

Four Capsule 3 UO_2 compacts were safety tested at temperatures ranging from 1500 to 1700°C. There was only one SiC failure at 1500°C, but there were substantial numbers of SiC failures from CO attack at higher test temperatures. The number of SiC failures at 1600°C ranged from several to dozens, and at 1700°C, there were hundreds of SiC failures. Despite the UO_2 SiC failures, no TRISO failures were observed in safety testing. The data are not conducive to accurately assessing particle failure fractions because of the relatively low number of total UO_2 particles that were safety tested. With no TRISO failures out of the 3086 UO_2 particles tested at 1600°C, the upper bound TRISO failure rate at 95% confidence is $\leq$9.7E-4. This is a relatively small sample size (compared to 19056 AGR-2 UCO particles safety tested at 1600°C), and more particles would have to be tested to more accurately assess the UO_2 TRISO failure rates.

Table 2. TRISO and SiC failure statistics for AGR-2 UCO fuel after safety testing at 1600 and 1800°C.

	Capsule	Temperature		Burnup (% FIMA)	Number of Particles	SiC			TRISO		
		TAVA (°C)	TA$_{max}$ (°C)			Number of Failures	Actual Failure Fraction	Failure Fraction Upper Bound [f]	Number of Failures	Actual Failure Fraction	Failure Fraction Upper Bound [f]
Irradiated [a]	All AGR-2 UCO	1142	1251	11.05	114336	6	5.25E-5	≤1.04E-4	≤4	≤3.50E-5	≤8.01E-5
1600°C Safety Tested [b]	2	1252	1360	12.17	6352	0	0	≤4.72E-4	0	0	≤4.72E-4
	5 & 6 combined	1088	1197	10.49	12704	0	0	≤2.36E-4	0	0	≤2.36E-4
	All AGR-2 UCO	1142	1251	11.05	19056	0	0	≤1.58E-4	0	0	≤1.58E-4
1800°C Safety Tested [c–e]	2 [c]	1252	1360	12.17	6352	1	1.57E-4	≤7.47E-4	0	0	≤4.72E-4
	5 & 6 combined [d]	1088	1197	10.49	9528	4	4.20E-4	≤9.61E-4	≤1	≤1.05E-4	≤4.98E-4
	All AGR-2 UCO [e]	1142	1251	11.05	15880	5	3.15E-4	≤6.62E-4	≤1	≤6.30E-5	≤2.99E-4

a. See Table 1.

b. No SiC or TRISO failures occurred in 1600°C safety tests of UCO fuel.

c. One SiC failure and no TRISO failures occurred in 1800°C testing of Capsule 2 compacts.

d. Only one Capsule 5 compact and one Capsule 6 compact suffered SiC or TRISO failures in 1800°C tests. One SiC failure and no TRISO failures occurred in Compact 5-4-1. Three SiC failures occurred in Compact 6-2-1. The possibility of one TRISO failure in Compact 6-2-1 was established by unusual release of ^{85}Kr and ^{134}Cs during safety testing, but no particles with failed TRISO were recovered to confirm that one failed-TRISO particle was present. If the true number of Compact 6-2-1 TRISO failures was zero, then the 95% TRISO failure fraction from combing the 1800°C safety test results of Capsules 5 and 6 would be ≤3.15E-4.

e. In combining all AGR-2 UCO data from 1800°C safety testing, the range of possible TRISO failures was from zero to one, and the number of possible SiC failures was five. If the true number of Compact 6-2-1 TRISO failures was zero, then the 95% TRISO failure fraction from all AGR-2 UCO 1800°C safety testing would be ≤1.89E-4 (not ≤2.99E-4).

f. Upper bound at 95% confidence.

2.1.1.6 Particle Morphologies and SiC Interactions with Fission Products and other Chemical Species

The types of morphologies observed in AGR-2 UCO fuel after safety testing for 300 h at temperatures from 1600 to 1800°C were generally the same as those observed in as-irradiated fuel. This is consistent with the fact that few SiC and TRISO failures occurred in the safety tests, attesting to the high-temperature stability of the fuel. In rare instances, degraded SiC was observed after 1800°C tests. In post-safety-test examinations of fuel particles with abnormally low Cs content after 1800°C tests, analysis by SEM and XCT revealed thinned or failed SiC layers caused by localized chemical reactions of the SiC with uranium and metallic fission products such as Pd. These metals reacted with the SiC to form metal silicides, leaving behind regions of high carbon content in the SiC layer. One TRISO failure at 1800°C was observed to have occurred as a result of chemical reactions between the TRISO coating and molybdenum contamination introduced during the fabrication process. This failure was not related to the inherent performance of the fuel.

Safety testing caused CO corrosion of SiC in UO_2 fuel such that the SiC layer failure rate in UO_2 was much higher than in UCO at all temperatures. Particles recovered and analyzed after safety testing revealed intergranular corrosion of the SiC layer via reaction with the excess CO produced in the UO_2 particles. Fission in UO_2 liberates excess oxygen that can react with the buffer to form CO that can react with SiC to form volatile SiO_2. In contrast, in UCO kernels, excess oxygen is consumed by reaction with the uranium carbide included with the uranium oxide for this purpose. Comparing the high-temperature performance of AGR-2 UCO and UO_2 fuels demonstrates that the UCO kernel chemistry successfully reduces CO production and eliminates SiC degradation via CO corrosion.

2.1.1.7 Fission Product Release from Safety-Tested Compacts

Releases of key radionuclides during safety tests of AGR-2 UCO fuel compacts were similar to those observed during safety testing of AGR-1 UCO fuel, and the maximum releases from AGR-2 compacts from Capsules 5 and 6 were somewhat lower than AGR-1 at 1800°C. Figure 2 summarizes the range of minimum and maximum fractional releases of key isotopes from safety-tested compacts. AGR-1 ranges are plotted as the base layer, and AGR-2 Capsules 5 and 6 data are overlaid on top of that. The AGR-2 Capsule 2 data are overlaid on top of the AGR-2 Capsules 5 and 6 data. The AGR-2 Capsule 2 fission product ranges are displayed separately from the other AGR-2 UCO capsules because the high irradiation temperature in Capsule 2 resulted in distinctly higher releases of ^{90}Sr and ^{154}Eu. AGR-2 Capsule 2 releases of ^{85}Kr, ^{134}Cs and ^{110m}Ag are similar to those from other AGR-1 and AGR-2 safety tests.

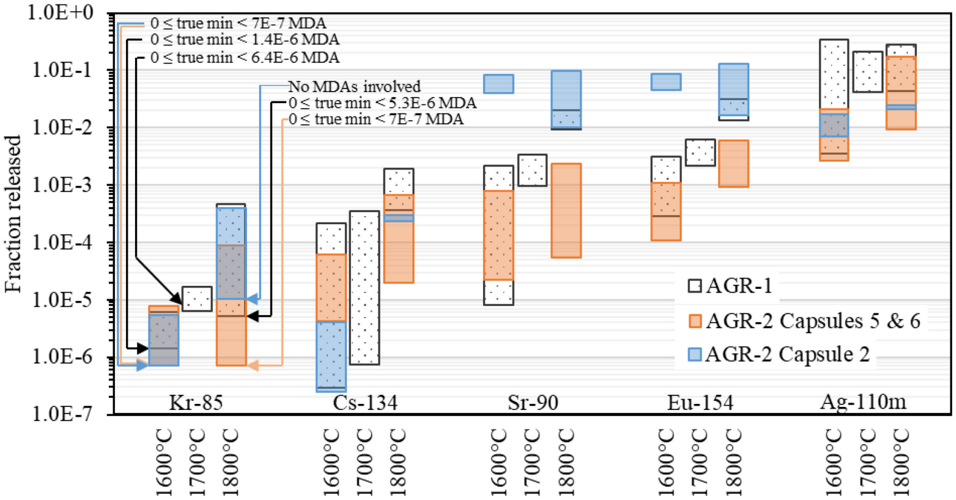

Figure 2. Range of compact fractions of key fission products released from safety-tested AGR-1 and AGR-2 UCO compacts.

Cesium is well retained by TRISO fuel with intact SiC layers. No SiC layer failures occurred in UCO fuel at 1600°C, and SiC layer failures were rare during 1800°C tests (Table 2). In the absence of particles with failed SiC layers, cesium releases were dominated by U contamination in the compact matrix from fabrication, and the measurements were further influenced by cesium picked up from contamination in the hot cell. At all temperatures, UCO ^{134}Cs releases were considerably less than UO_2 ^{134}Cs releases because SiC failures were observed in all UO_2 tests.

In the absence of particles with compromised coating layers, krypton releases were generally very low and were often below the minimum detection limits for ^{85}Kr in UCO and UO_2 fuel safety tests. Small amounts of Kr can diffuse through the OPyC in particles with degraded or failed SiC layers. Trace levels of Kr could have come from uranium contamination present in the compacts at the time of fabrication.

In most UCO and UO_2 safety tests at temperatures ≤1600°C, the majority of the ^{110m}Ag release occurred at the very beginning of the tests. Some of this Ag came from what had been released in-pile through intact TRISO coatings that was still retained in compact matrix material after irradiation, but some additional release through intact TRISO coatings also occurred. In some cases, it was apparent that much of the measured ^{110m}Ag releases had occurred via diffusion through intact TRISO coatings during the 12-hour pause at 1250°C prior to ramping to the final test temperature. At safety-test temperatures of 1600 and 1700°C, releases of ^{110m}Ag from UO_2 fuel were dominated by elevated SiC failure rates. Releases of ^{110m}Ag from UO_2 fuel at 1500°C were similar to those from UCO fuel during 1600°C tests, in which the more-likely release mechanisms were via the inventory retained in the compact matrix and diffusion through intact particles.

Safety-test releases of ^{154}Eu were dominated by the inventory that had been released through intact TRISO particles during irradiation that was retained in the compact matrix after irradiation, and fuel compacts with higher irradiation temperatures (e.g., Capsule 2 compacts) were shown to have higher matrix inventories of ^{154}Eu. Capsules 5 and 6 fuel had significantly lower irradiation temperatures than Capsule 2, and ^{154}Eu releases from safety tests of Capsules 5 and 6 fuel were one to two orders of magnitude lower than in Capsule 2 safety tests. Synthesizing the results of as-irradiated compact DLBL, safety tests, and post-safety test data from similar compacts indicates that ^{154}Eu release from failed SiC layers (which had very low failure rates) or from slow diffusion of ^{154}Eu through intact SiC coatings during the safety test were only small contributors to ^{154}Eu release from safety-tested UCO fuel compacts. In Capsules 5 and 6 compacts, which had lower irradiation temperatures, and lower matrix inventories of ^{154}Eu after irradiation, ^{154}Eu releases from intact particles may have comprised a larger portion of the total release than in the hotter Capsule 2 compacts. The Eu releases from UO_2 fuel compacts with SiC failures that occurred at 1600°C were comparable to releases from Capsule 6 UCO compacts (with similar burnups and higher irradiation temperatures than the UO_2 compacts) that were tested at 1600°C and had no SiC failures. Thus, UCO and UO_2 compacts with similar irradiation histories retained ^{154}Eu to a similar degree during 1600°C safety tests.

In safety tests of UCO fuel from Capsules 2 and 5, the ^{90}Sr releases paralleled the ^{154}Eu releases, and total releases of ^{90}Sr at the end of these tests were just a little lower than the total ^{154}Eu releases. Similar to the behavior observed for ^{154}Eu, total amounts of ^{90}Sr released from safety testing were higher from compacts with higher irradiation temperatures due to increased matrix inventories of ^{90}Sr in fuel that had higher irradiation temperatures. The time-dependencies of the ^{90}Sr releases from UO_2 safety tests were remarkably similar (albeit at lower values) to the Cs releases from UO_2 fuel safety tests. This indicates that ^{90}Sr release from UO_2 compacts was dictated by SiC failures, which were encountered in all UO_2 safety tests. Europium releases from UO_2 fuel safety tests were lower and did not parallel the release of faster-transporting Cs. This suggests that UO_2 compacts were less retentive of Sr than Eu at safety-test temperatures. Releases of ^{90}Sr from UCO Compact 6-2-2 at 1600°C were similar to those of UO_2 Compact 3-1-1 at 1500°C. The ^{90}Sr releases from safety tests of UCO Compacts 6-4-2 (1600°C) and 6-4-3 (1800°C) were about 10 to 20× less than the releases from UO_2 Compacts 3-3-2 and 3-4-2 safety tests at 1600°C. This indicates that UCO fuel compacts with higher burnups and irradiation temperatures retain Sr better at safety test temperatures than UO_2 fuel.

2.1.1.8 Temperature Transient Safety Test of UCO Compacts

Three AGR-2 Capsule 5 UCO compacts were safety tested using a time-varying temperature profile to simulate a depressurized conduction cooldown (DCC) event with a peak temperature of 1695°C. This test was performed in a similar manner to a previous test using three AGR-1 UCO compacts. In a prior test of irradiated German UO_2 fuel pebble AVR-91/31, a higher rate of particle failures was observed during such a test. In the AGR-1 and AGR-2 tests, no SiC or TRISO failures were observed. This indicates that the temperature transient does not impose additional stress on UCO fuel beyond that demonstrated in the isothermal heating tests. In fact, the temperature variations during this simulated core-conduction cooldown transient temperature heating test caused less release of ^{154}Eu, ^{85}Kr, and ^{90}Sr than in the 300-hour isothermal tests at 1600°C.

2.1.2 AGR-3/4 Radial Deconsolidation

Compacts in the AGR-3/4 irradiation campaign were fabricated with 20 designed-to-fail (DTF) particles distributed vertically through the compact centerline, as shown in Figure 3. These DTF particles consisted of a 350-µm diameter uranium carbide/uranium oxide (UCO) kernel coated with only a single layer of PyC instead of the typical series of layers included in TRISO particles. To promote failure during irradiation, the DTF PyC layer was intentional designed to be thinner (20 vs. 40 µm), denser (1.98 vs 1.90 g/cm^3), and with a higher optical anisotropy factor (1.24 vs. 1.02) than normal TRISO PyC (Hunn et al. 2012). The intent of this inclusion was that the failure of the PyC coating in the early stages of irradiation would create a line source of known intensity of actinides and fission products to study their diffusion in the compacts and surrounding materials. Concentration profiles of individual fission products and actinides within the irradiated compacts were measured during PIE by electrolytically deconsolidating the rotating compacts into a series of radial fractions using the apparatus shown in Figure 3, then performing LBL and radiochemical analysis. In addition, random samples of particles from some compacts were counted using the IMGA to determine the particle inventory statistics for key radioisotopes. Detailed results from this work were submitted in the FY 2021 Level 3 milestone report “Radial Deconsolidation and Leach-Burn-Leach of AGR-3/4 Compacts 8-4 and 7-4”, ORNL/TM-2021/2178 (Helmreich et al. 2021) and excerpts from that report are summarized or reproduced herein.

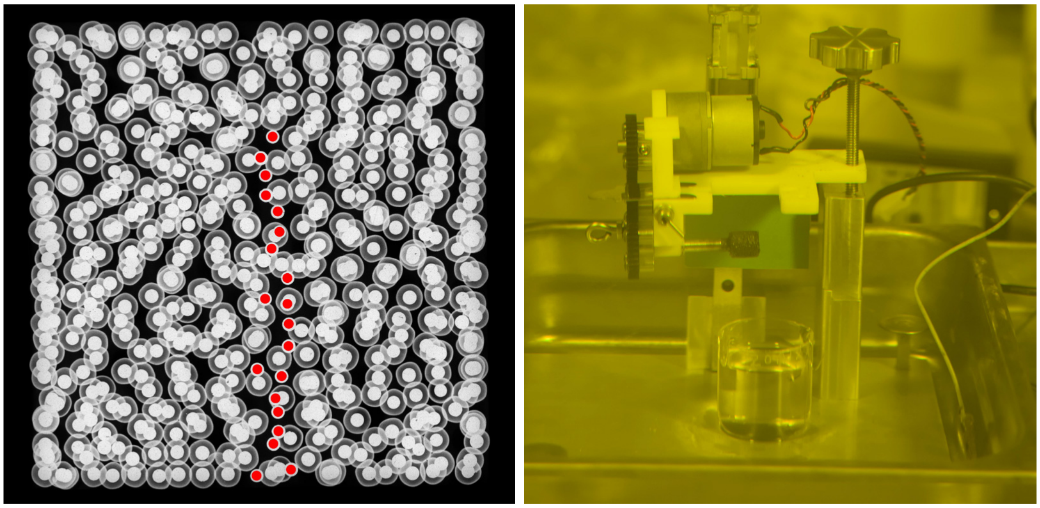

Figure 3. X-ray radiograph of and AGR-3/4 compact with DTF particles shown in red (left) and radial deconsolidation rig used to divide compacts into radial segments (right).

Three concentric cylinders of driver fuel particles and matrix were removed from Compact 8-4 by radially deconsolidating the compact in three stages. The remaining cylindrical core encompassing the DTF particles was then axially deconsolidated. Table 3 shows the actual segment dimensions and volumes for Compact 8-4 as determined by automated image analysis of the set of 50 photos of the rotating compact acquired before and after each segment. The removal of material was generally uniform along the compact, resulting in an approximately cylindrical remainder after each segment. The deconsolidated material and acid from each segment were analyzed using an LBL process with a Soxhlet extractor as has been previously reported (Hunn et al. 2013; Hunn and Montgomery 2020) with minor adjustments. The inventory data in particle-equivalents for select isotopes of actinides and fission products are given in Table 4.

Table 3. Segment results for Compact 8-4 measured with automated photo analysis

Quantity	**Segment 1**	**Segment 2**	**Segment 3**	**Segment 4**
Initial diameter (mm)	12.126	10.858	9.186	6.798
Residual diameter (mm)	10.858	9.186	6.798	0
Segment thickness (mm)	0.634	0.836	1.194	solid
Segment volume (cm^3)	0.286	0.329	0.375	0.454
Deconsolidation time (min)	28	23	25	

Table 4. Comparison of particle-equivalents of select nuclides in Compact 8-4 segments

Nuclide	**Segment 1**	**Segment 2**	**Segment 3**	**Segment 4**	**Total**
^{235}U	(0.416)	(1.048)	(0.955)	(14.938)	(17.357)
^{239}Pu	(0.401)	(0.603)	(0.671)	(14.618)	(16.293)
^{144}Ce	(0.184)	(0.217)	(0.344)	(17.724)	(18.469)
^{137}Cs	(0.090)	(0.190)	(0.132)	(2.162)	(2.574)
^{90}Sr	(5.030)	(5.974)	(8.948)	(12.384)	(32.336)
^{154}Eu [a]	(6.274)	(6.738)	(10.617)	(15.290)	(38.919)

[a] Values for ^{154}Eu were adjusted for offset in calculated inventory by dividing by the average measured-to-calculated ratio (0.89) for particles from Compacts 1-4, 10-4, and 7-4 which were gamma counted using IMGA.

Three annular rings of driver fuel particles and matrix were removed from Compact 7-4 by radially deconsolidating the compact in three stages. The remaining cylindrical core encompassing the DTF particles was then axially deconsolidated. The third radial deconsolidation segment of Compact 7-4 was cut short by the compact separating from the rotating axle, rendering further radial deconsolidation impossible. It was decided that the volume of the third segment was too small to be analyzed on its own, so the particles, matrix debris, and acid from the third radial deconsolidation were combined with those from the final deconsolidation of the remaining solid compact. This final deconsolidation step required the use of a special deconsolidation rig to hold the residual compact partially submerged in nitric acid while completing the electrolytic circuit. Table 5 shows the actual segment dimensions and volumes for Compact 7-4 as determined by the automated image analysis, and the inventory data in particle-equivalents for select isotopes of actinides and fission products are given in Table 6. Note that the higher inventory of ^{235}U, ^{239}Pu, ^{144}Ce, and ^{137}Cs in Segment 1 vs. Segment 2 indicates that one driver fuel particle was broken during radial deconsolidation.

Table 5. Segment results for Compact 7-4 measured with automated photo analysis

Quantity	Segment 1	Segment 2	Segment 3
Initial diameter (mm)	12.09	10.61	9.10
Residual diameter (mm)	10.61	9.10	0
Segment thickness (mm)	0.74	0.76	Solid
Segment volume (cm^3)	0.33	0.29	0.81
Deconsolidation time (min)	44	20	54

Table 6. Comparison of particle-equivalents of select nuclides in Compact 7-4 segments

Nuclide	Segment 1	Segment 2	Segment 3	Total
^{235}U	(1.220)	(0.232)	(14.666)	(16.118)
^{239}Pu	(1.980)	(0.494)	(14.257)	(16.731)
^{144}Ce	(1.298)	(0.277)	(17.089)	(18.664)
^{137}Cs	(1.046)	(0.249)	(4.741)	(6.036)
^{90}Sr	(10.190)	(8.909)	(22.138)	(41.237)
^{154}Eu [a]	(13.710)	(11.960)	(26.458)	(52.128)

a. Values for ^{154}Eu were adjusted for offset in calculated inventory by dividing by the average measured-to-calculated ratio (0.92) from the 45 Compact 7-4 particles that were gamma counted with IMGA.

All 1849 driver fuel particles recovered from Compact 7-4 were surveyed using IMGA. Two low-inventory particles from Segment 3 were culled out in accordance with the IMGA particle sorting algorithms. The broken driver fuel particle apparent in Segment 1 from the LBL results was not recovered with TRISO coatings in one piece. Longer gamma counting showed that one of the low-inventory Segment 3 particles was a normal particle with a smaller-than-average kernel, while examination using x-ray computed tomography (Figure 4) showed that the other was a cracked shell with approximately one third of the coating layers missing and no kernel remaining, which indicated that Segment 3 also had a broken TRISO particle.

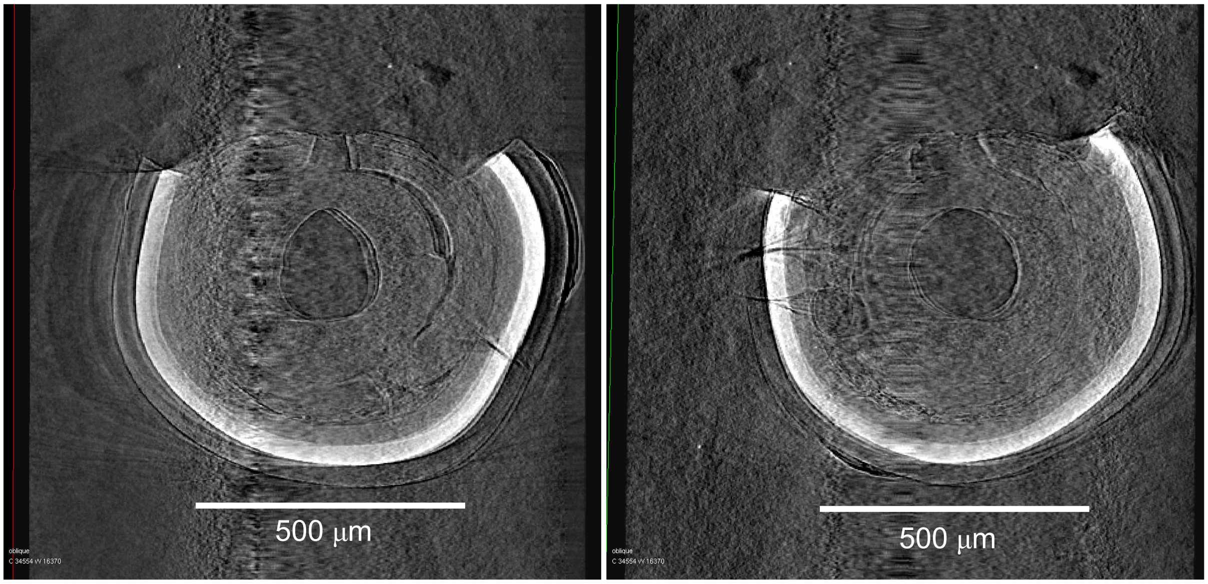

Figure 4. Orthogonal tomograms of the cracked driver fuel particle recovered from Compact 7-4 Segment 3.

After the initial IMGA survey, 15 particles were randomly selected from each Compact 7-4 segment population for extended gamma counting of 4 h each. Table 7 shows the means and standard deviations (SDs) of the combined sample of 45 RS particles. No outliers were identified within these 45 particles, and mean values were near unity (within the uncertainties in the analysis and calculated inventories) with the exception of ^{125}Sb and ^{154}Eu, which had offsets relative to their calculated inventories as has been previously observed in all AGR tests.

Table 7. Statistical summary of Compact 7-4 driver fuel particle activities

	Value	**^{106}Ru**	**^{125}Sb**	**^{134}Cs**	**^{137}Cs**	**^{144}Ce**	**^{154}Eu**
Mean	Bq	1.53E+07	2.10E+05	5.03E+06	4.07E+06	5.79E+07	1.46E+05
Mean	M/C	1.11	0.68	0.98	1.04	1.00	0.92
SD	Bq	9.2%	9.2%	8.1%	8.0%	8.3%	8.0%
SD	M/C	4.2%	4.0%	1.7%	-	3.4%	6.0%

Note: M/C is the measured-to-calculated ratio of a radionuclide in a measured particle divided by the normalized 137Cs inventory in that particle.

The average concentrations of select actinides and fission products in particle-equivalents per cubic centimeter were calculated for each segment of AGR-3/4 Compacts 8-4 and 7-4 and compared to data generated in the same manner for AGR-3/4 Compact 1-4 from (Hunn et al. 2020). The estimated contributions from the broken driver fuel particles in Compact 7-4 were subtracted before calculating the average concentrations in each segment of that compact. Comparison of the results between these compacts alludes to the influence of irradiation temperature on fission product transport as they span a range of irradiation TAVA temperatures of 929, 1169, and 1319°C for Compacts 1-4, 8-4, and 7-4 respectively.

A comparison of concentration profiles for ^{144}Ce and ^{137}Cs for all three compacts is given in Figure 5. The concentration profiles for ^{144}Ce and ^{137}Cs in all three compacts mostly followed the expected decreasing trend toward the outside of the compact due to diffusion from the source term of DTF particles in the compact cores. However, the total inventory of ^{137}Cs was significantly low in the two compacts irradiated at higher temperature. This depletion in the higher irradiation temperature compacts was likely due to diffusion of ^{137}Cs out of the compacts and is supported by measurements of the ^{137}Cs inventory in the capsule rings and hardware (Stempien et al. 2018). While less pronounced, the slightly lower ^{144}Ce inventory measured in Compact 7-4 (the hottest compact) also suggested more out-diffusion and release from the compact.

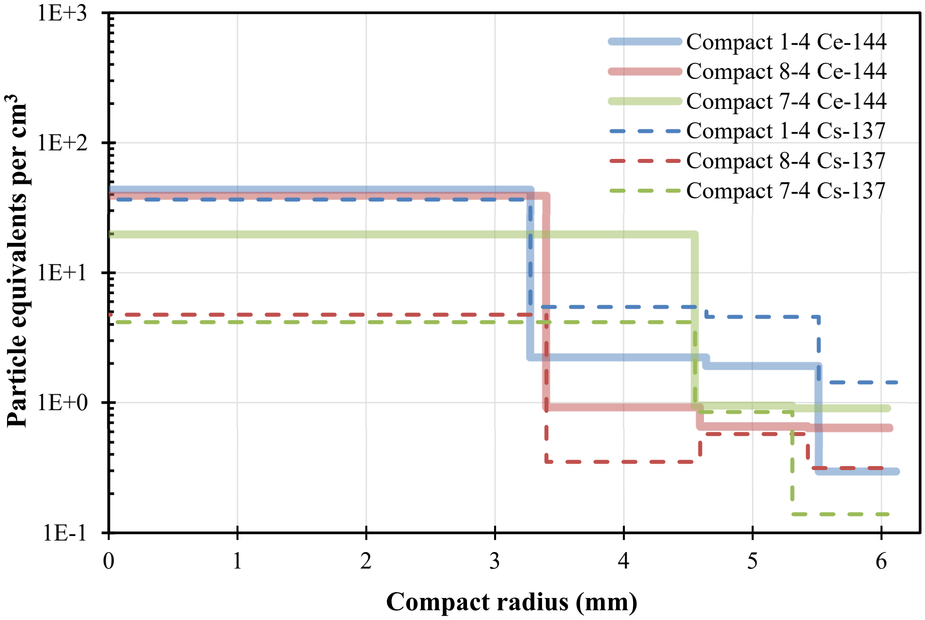

Figure 5. Concentration profiles of ^{144}Ce and ^{137}Cs in Compacts 1-4, 8-4, and 7-4.

A comparison of the concentration profiles for ^{154}Eu and ^{90}Sr for all three compacts is given in Figure 6. While the concentration profiles for these isotopes in Compact 1-4 followed the expected progressively decreasing trend associated with diffusion from DTF particles in the compact core, the concentration profiles for Compacts 8-4 and 7-4 were nearly flat. These flat concentration profiles along with the higher total inventories of ^{154}Eu and ^{90}Sr found in the higher irradiation temperature compacts indicate significant temperature-dependent release of these isotopes from the driver fuel particles. Substantial additional ^{154}Eu was found in the Capsule 7 and 8 rings and hardware (Stempien et al. 2018). The fact that the ^{154}Eu and ^{90}Sr releases through intact SiC in the driver fuel particles followed similar temperature-dependent trends is consistent with observations from AGR-1 and AGR-2 PIE and safety testing, where releases of these elements tend to track together as a function of temperature (Demkowicz et al. 2015; Stempien et al. 2021). This has been related to the fact that these elements both form carbides in the UCO fuel system.

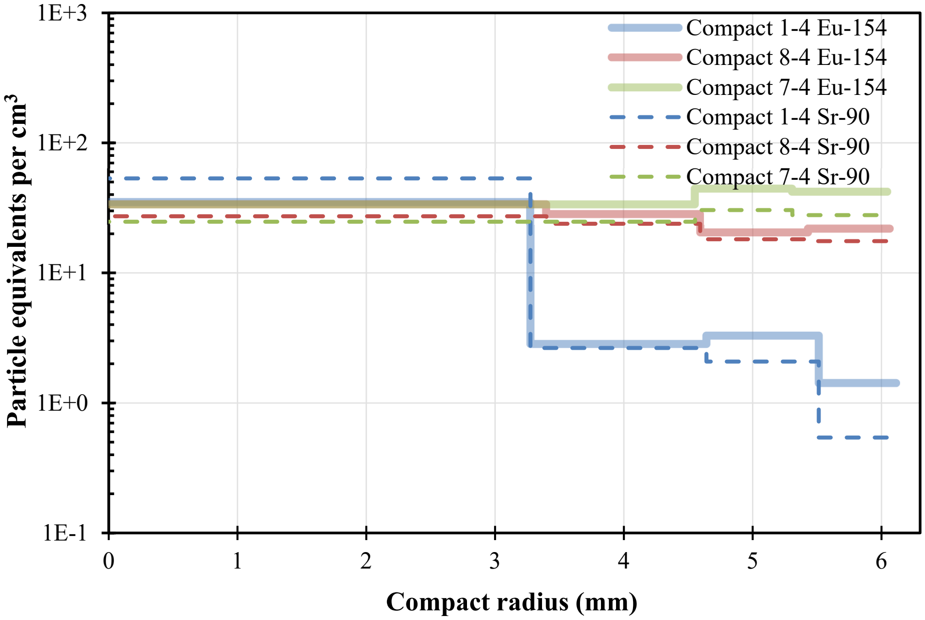

Figure 6. Concentration profiles of ^{154}Eu and ^{90}Sr in Compacts 1-4, 8-4, and 7-4.

A comparison of the concentration profiles for ^{235}U and ^{239}Pu for all three compacts is given in Figure 7. In Compact 1-4 the concentration profiles for ^{235}U and ^{239}Pu followed the expected decline with each segment moving out from the compact core, and the total inventories of both isotopes were near the nominal 20 particle-equivalents expected from the DTF particles. In contrast, the concentration profiles of ^{235}U and ^{239}Pu in Compacts 8-4 and 7-4 were relatively flat outside of the compact cores and the total compact inventories for these actinide isotopes were lower than expected. These results suggest that while these actinides were mostly stable in the remnants of the failed DTF particles within the core segments, a temperature-dependent fraction was released from the DTF kernels and diffused out of the compacts. This behavior was similar and somewhat more advanced compared to what was observed for ^{144}Ce in Compact 7-4.

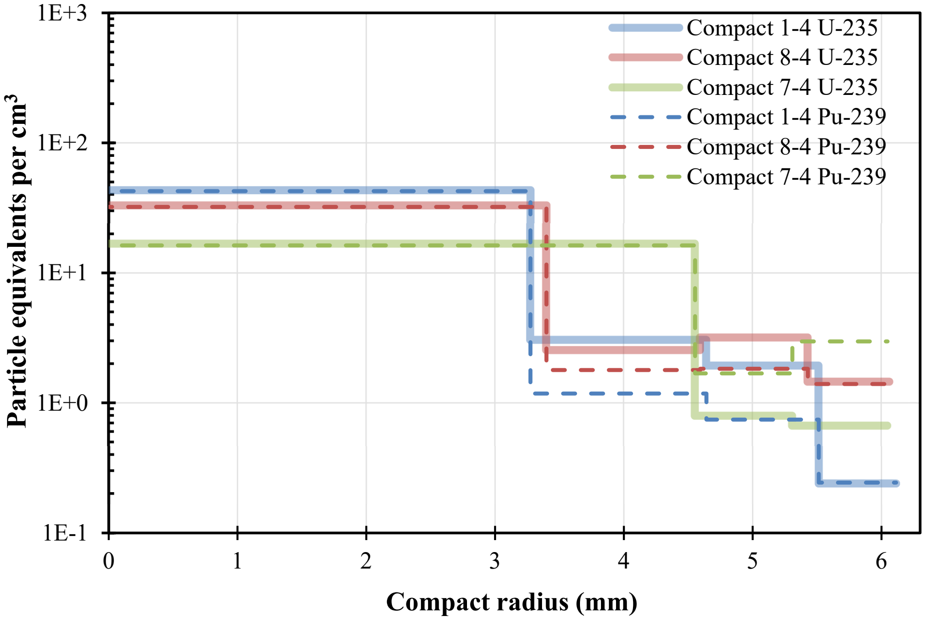

Figure 7. Concentration profiles of ^{235}U and ^{239}Pu in Compacts 1-4, 8-4, and 7-4.

2.1.3 FITT Oxidation Studies

As part of the AGR-2 post-irradiation examination effort, the response of irradiated TRISO particles under oxidizing environments was explored. Results were captured in the FY2021 Level 3 milestone report "Oxidation Testing and Examination of AGR-2 TRISO Particles," ORNL/TM-2021/2092 (Skitt et al. 2021). Individual particles from AGR-2 Compact 5-4-2 with their OPyC) layer removed were exposed in the FITT to understand particle failure and oxide growth as a function of exposure time. The results provide support for future integral oxidation tests in the INL Air/Moisture Ingress Experiment and direct insight into the influence of irradiation on oxidation kinetics. The particle exposures were conducted in FITT after the system was modified to support oxidation testing, as the initial configuration was developed to support long-term thermal testing of irradiated TRISO particles in inert atmospheres. The goals of these tests were to measure particle failure rate and time to failure as a function of exposure time, understand oxidation behavior of the SiC layer in irradiated and unirradiated particles for varying exposure durations at 1400°C, analyze oxidation microstructure in individual particle samples, and develop insights on differences in oxidation kinetics of irradiated SiC relative to those of unirradiated SiC. The following summary of the individual particle oxidation testing was derived from Skitt et al. (2021).

Irradiated particles from Compact 5-4-2 were selected for FITT oxidation studies and were compared with unirradiated particles from Compact LEU09-OP2-Z002 (Hunn et al. 2010). The details of Compact 5-4-2 irradiation conditions are found in Table 8. Compact 5-4-2 was targeted as it represented average irradiation conditions (e.g., burnup and temperature) among AGR-2 compacts. Prior to testing, the particles were liberated from their respective compacts. The Compact 5-4-2 particles were subjected to a standard DLBL process, which included a burn step of 750°C for 72 h in air. The as-fabricated compact was deconsolidated, and particles were burned in air at 750°C for 72 h followed by a 24-h acid leach and rinse. This process resulted in "burn-back" particles with an exposed SiC outer surface and no OPyC coating. Thus, the oxidation testing was a direct observation of oxidation response of the exposed SiC layer. For each test, ten irradiated and ten unirradiated particles were placed in a 3D printed SiC cup with a divider that separated the two types of particles. The SiC cup was placed in an alumina holder that nested in the bottom of a closed-end alumina tube. The closed-end tube was sealed with a Cajon fitting at the top that had an alumina flow tube passing through to deliver the oxidant. Prior to operations, the internal volume was evacuated and purged with inert gas. The system was brought up to the soak temperature under flowing inert gas, after which the oxidant gas was introduced at a flow rate of 50 mL/min to begin the test (the total internal volume of the system was ~321 mL). Details of the testing apparatus can be found in Skitt et al. (2021).

Table 8. Irradiation conditions for AGR-2 UCO Compact 5-4-2

Compact ID [a]	**Fabrication ID** [b]	**Fuel type**	**Average burnup** [c] **(FIMA)**	**Fast fluence** [c] **(E > 0.18 MeV)**	**TAVA Temperature** [d]
AGR-2 5-4-2	LEU09-OP2-Z059	UCO	12.03%	3.14×10^{25} n/m^2	1071°C

[a] The X-Y-Z compact identification (ID) convention denotes the location in the irradiation test train: Capsule-Level-Stack.

[b] Physical properties data for individual compacts are available and referenced to fabrication ID (Hunn, Montgomery, and Pappano 2010, pages 60–69).

[c] Burnup in FIMA and fast neutron fluence are from physics calculations (Sterbentz 2014).

[d] tc temperature is based on thermal calculations (Hawkes 2014).

Table 9 lists the test condition run in FY2021; however, characterization has not been completed on particles from all conditions at the time of this reporting. After each test condition particles were extracted from furnace internals. For the 1400°C, 100–400-h and 1200°C, 400-h exposures, the particles were retrieved after transfer to a glove box where particle ID was not maintained. Surviving particles were isolated and transferred to the hot cell for individual particles gamma analysis using standard IMGA procedures. The IMGA analysis served to identify intact irradiated and unirradiated particles after exposure. Randomly selected particles were then mounted for FIB and SEM analysis. This analysis focused on surface oxide imaging and analysis of oxide thickness by milling cross sections with the FIB. A novel image processing routine was developed to automate the measurement of the oxide layer in cross section by applying a mask to the region of interest as shown in Figure 8. Select locations of interested were targeted for analysis by fabricating lamellae for scanning transmission electron microscopy (STEM). The STEM analysis explores the crystal structure and composition of the oxide layer to provide support to oxide thickness observations. At the time of this reporting IMGA and SEM analysis on all 1400°C conditions have been completed along with STEM analysis of the 1400°C 50 and 100 h conditions. These observations have been reported in Skitt et al. (2021).

Table 9. Oxidizing test conditions for irradiated and unirradiated particles completed in FY21

Temperature	**Atmosphere**	**Exposure Time**			
1400°C	21% O_2 (balance N_2)	50 h	100 h	200 h	400 h
1200°C	21% O_2 (balance N_2)				400 h

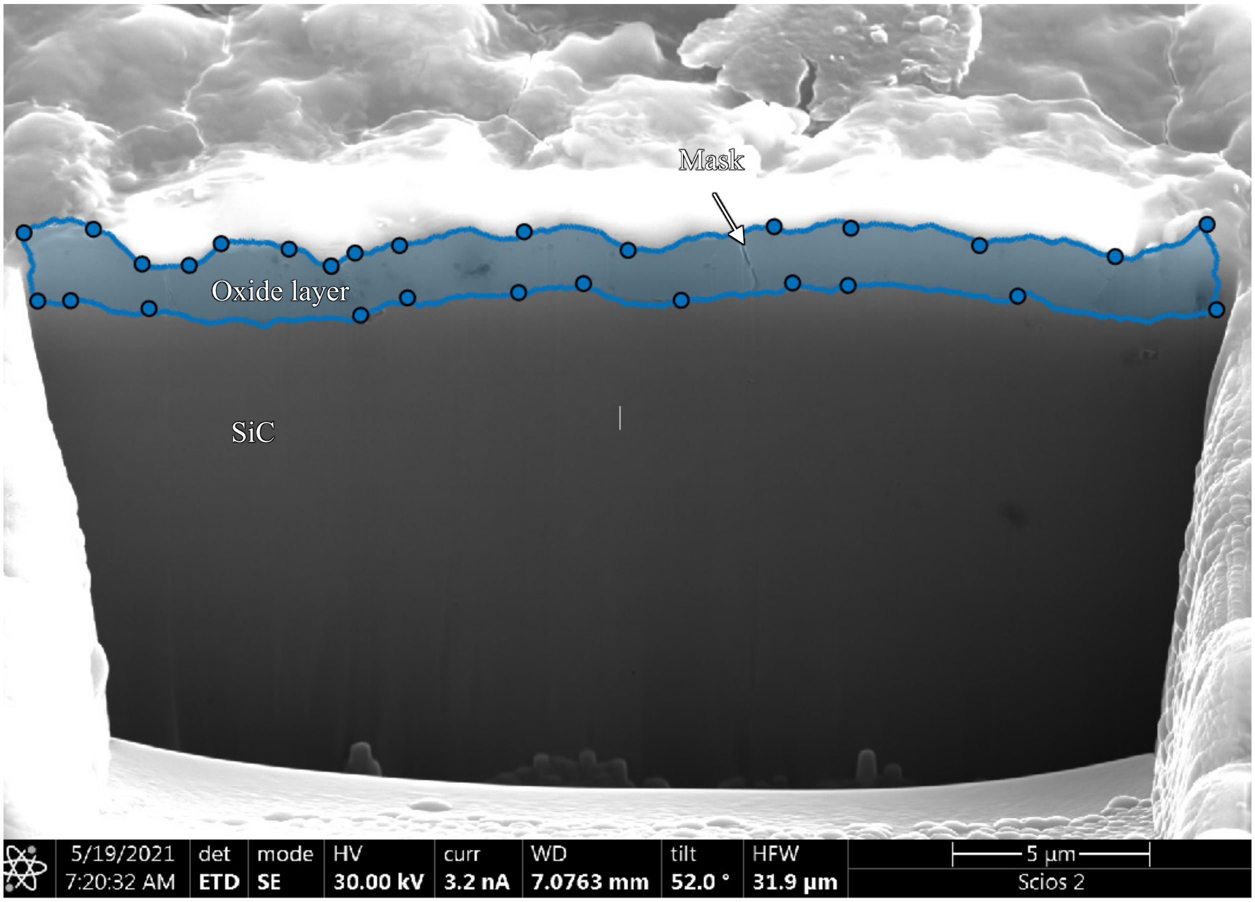

Figure 8. Example of mask applied over oxide layer to support automated thickness measurements.

2.1.3.1 Particle Failure Analysis

Particle failure fraction as a function of exposure time was determined based on direct observation of recovered particles and gamma analysis using the IMGA. As such, the unrecovered particles represent the general failure fraction for each exposure condition. Figure 9 presents the failure fraction as a function of exposure time at 1400°C. Direct counting of recovered particles determined gross failure fraction. No failures were observed after the 1400°C, 50-h exposure. Gross failures were observed in 100–400-h exposures and were indicated by complete loss of a particle. In some instances where gross failure was observed, residual particle material was identified such as debris and SiC fragments. Recovery of this residual material was speculated to be impacted by bonding with the SiC cup and limitations of the stereoscope in the IMGA cell. The IMGA analysis of the recovered particles showed no evidence of fission product release (Skitt et al. 2021), which would be indicative of a failed SiC or exposed-kernel defect in an intact particle.

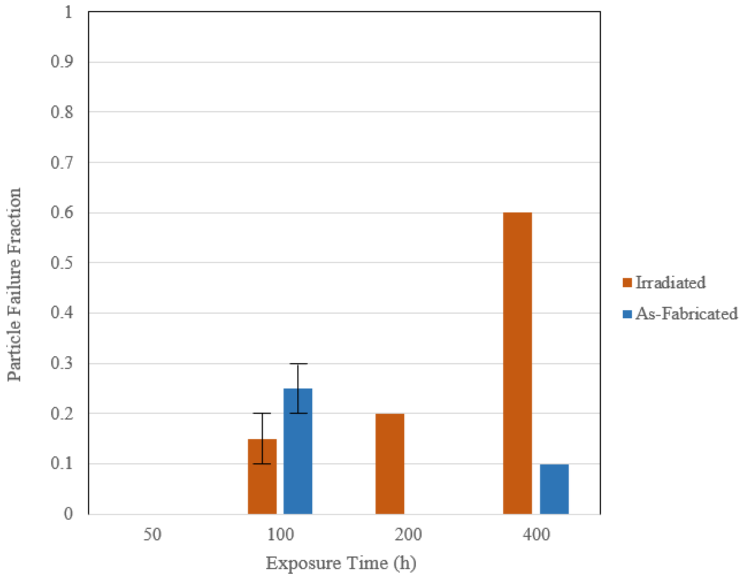

Figure 9. Particle failure fraction versus exposure time at 1400°C.

Figure 9 shows the failure rate as a function of exposure time at 1400°C. The error bars on the 100-h exposure represent the possible range in failure fraction, as one particle was lost during IMGA counting and could not be identified as irradiated or unirradiated. The analysis showed a baseline subset of particles was susceptible to failure under oxidizing conditions regardless of irradiation status, as indicated by the unirradiated particle failures in the 100 h and 400 h exposures. Based on previously reported oxidation response, an increase in failure was expected after ~400 h for irradiated TRISO (not burn-back) particles (Moormann 2011; International Atomic Energy Agency (IAEA) 1997). A similar trend was noted in this work where an increased failure fraction was measured for the irradiated particles after 400 h. The 60% failure fraction was above the baseline failure rate observed for the 100–200 h exposures, which suggests a real increase in failure fraction. This analysis indicates an increase in susceptibility for particle failure for irradiated particles relative to unirradiated particles after 400 h at 1400°C under oxidizing conditions (21% O_2).

2.1.3.2 SiC Oxidation Response

The comparison of unirradiated and irradiated particles provides a direct insight into the impact of irradiation on SiC oxidation response. The analysis showed a variable response of the oxide structure between the unirradiated and irradiated samples for the 50–100 h exposures at 1400°C. This is shown in Figure 10 for the 1400°C, 50-h exposure in which uniform oxidation was observed for both particles but the external surface varied between the two sample types. Specifically, a textured, fine-grained surface was noted for the unirradiated particles compared with a more uniform surface with cracks observed for the irradiated particles. The difference in the oxide structure was further confirmed by supporting TEM analysis which revealed the crystal structure of the two samples was different, with the irradiated particles showing a crystalline structure and the unirradiated particles having an amorphous oxide layer. The oxide layers after 200 and 400-h exposures were more complex than after 50–100 h exposures. Figure 11 shows the SEM analysis of the 400 h samples. The cross sections reveal a nonuniform oxide structure with large bubbles near the outer surface and more uniform structure towards the oxide/SiC interface. Note a nonuniform secondary oxide layer was observed in the particles subjected to 100–400 h exposures and was speculated to be associated with contact points with the SiC cup. The analysis presented here focuses on exploring the uniform oxide layers away from these contact points (Skitt et al 2021).

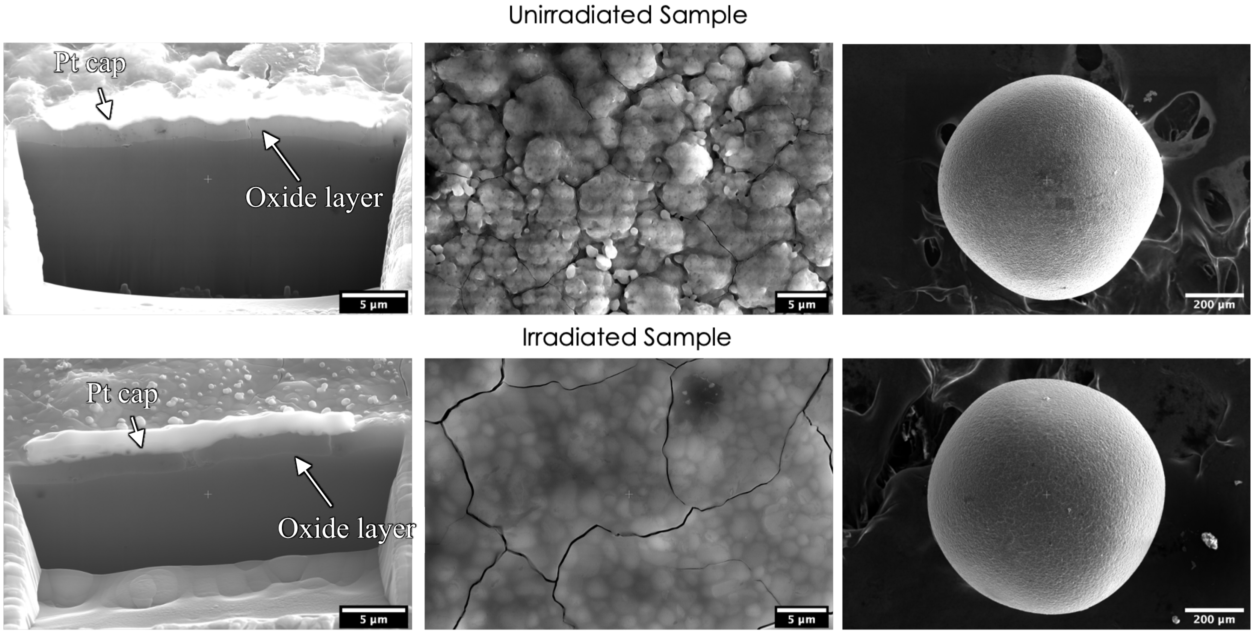

Figure 10. Cross section and surface images of the 50-h unirradiated and irradiated FITT samples.

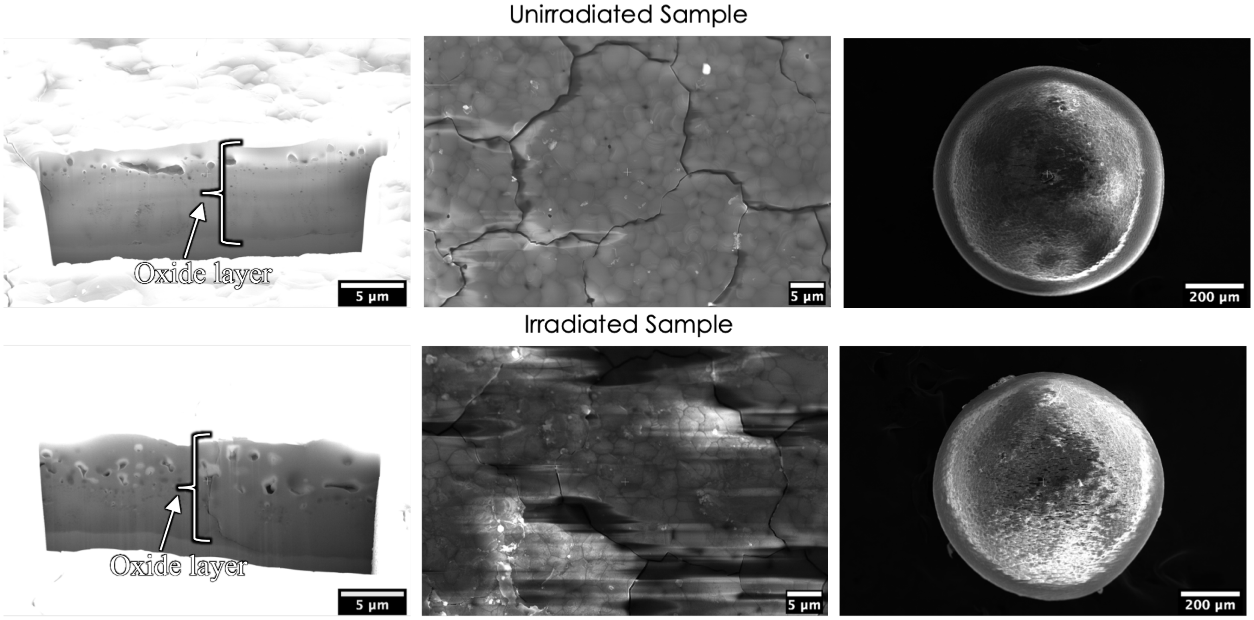

Figure 11. Cross section and surface images of the 400-h unirradiated and irradiated FITT samples. Charging on the irradiated sample caused blurring of the sample surface image.

The FIB cross sectioning provided information on average oxide thickness for each sample type at each exposure time. Table 10 lists the average measured oxide thicknesses. A general trend of increasing oxide thickness was observed with increasing exposure time. This is expected as oxide growth is a kinetic process. Compared with the unirradiated particles, the oxide thickness was apparently thinner for the irradiated particles at 50–100 h but thicker after the 400-h exposure.

Table 10. Oxide thickness for unirradiated and irradiated burn-back particles after exposure to 50–400 h.

Exposure Time (h)	**Average Thickness (µm)**	
	Unirradiated	**Irradiated**
50	1.74 ± 0.26	1.65 ±0.11
100	2.34 ± 0.28	1.88 ± 0.27
200	3.58 ± 0.18	3.44 ± 0.29
400	7.47 ± 0.19	8.29 ± 0.47

The oxide thickness data were used to explore the oxidation rates for each particle type. A detailed description of the oxidation kinetics evaluation is presented in Skitt et al. (2021). Most studies exploring oxidation of SiC in the passive regime explore oxidation over the course of tens of hours (Narushima et al. 1997). The oxidation response generally shows a parabolic response. A simple treatment of parabolic oxidation rates can be determined based on the relationship $x^2 = Bt$ where x is the oxide thickness (µm), t is time (h), and B is the parabolic rate constant (µm^2/h). Linear regression analysis can be used to determine B when plotting the square of the oxide thickness versus exposure time. Figure 12 shows linear fits for each particle type (irradiated and unirradiated) over 50–200 h and 50–400 h ranges while Table 11 shows the calculated parabolic rate constants over various exposure ranges for both particle types. From Figure 12, a breakdown in the linear fit was observed over the 50–400 h range relative to the 50–200 h range, and this is reflected in the decreasing R^2 values when including the 400 h data (Table 11). This indicates that the oxidation behavior beyond 200 h no longer follows a parabolic behavior. This breakdown from parabolic behavior was not surprising considering the long exposure times. Deviations from parabolic behavior have been observed at high temperatures and long exposure times as breakdown of the oxide layers can lead to "enhanced oxidant transport" as reported by Costello and Tressler (1986).

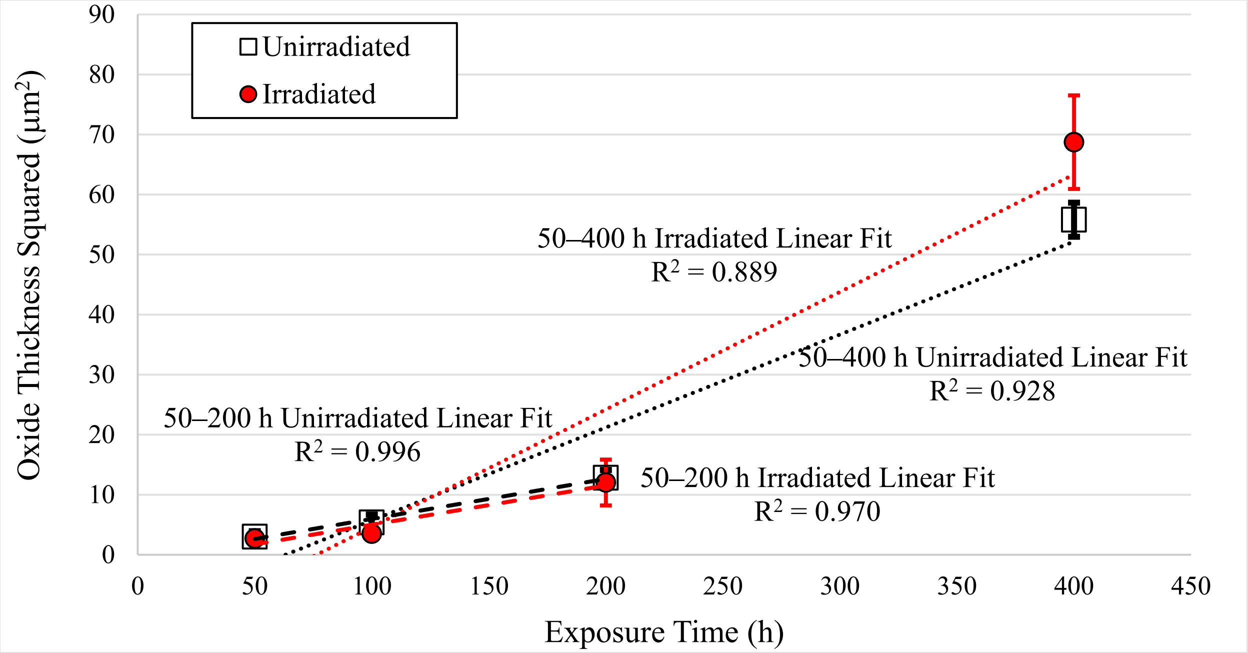

Figure 12. Oxide thickness squared versus exposure time.

Table 11. Best-fit parabolic rate constants for different exposure ranges.

Exposure Time Range (h)	Unirradiated		Irradiated	
	B (μm2/h)	R^2	B (μm2/h)	R^2
50–100	0.055	0.998	0.039	0.963
50–200	0.062	0.996	0.055	0.970
50–400	0.120	0.928	0.143	0.889

The parabolic oxidation rate constants over the range of 50–400 h at 1400°C were on the order of those reported by Cao et al. (2020) and Liu et al. (2014) for TRISO particles at 1400°C of 0.121 and 0.126 $\mu m^2/h$, respectively. However, the deviation from a linear fit observed in the FITT study implies that the behavior was not parabolic over the entire range of 50–400 h. Parabolic rate constants of 0.055 and 0.062 $\mu m^2/h$ over the 1400°C, 50–200 h exposure from this study better match those reported by Cao et al. (2020) and Liu et al. (2014) for 1300°C of 0.042 and 0.058 $\mu m^2/h$, respectively. The difference in the reported oxidation rates could be due to differences in experimental setup (e.g., when oxidant was introduced), materials, or temperature control. The measured oxidation rates reflect an inversion in the relative oxide thickness between the irradiated and unirradiated conditions from the 50–100 h and 400 h exposures. A lower parabolic rate constant for the irradiated particles is supported by the oxide analysis reported by Costello and Tressler (1986) in which oxidation was faster in amorphous oxide layers compared to crystalline oxide layers. Amorphous layers, as observed in the unirradiated particles, support faster diffusion of the oxidant and lead to increased oxidation relative to crystalline layers as observed in the irradiated particles. For the longer exposures, it is speculated that the breakdown of the oxide layer and influence of impurities due to irradiation (e.g., transmutation products and fission products) may support higher average diffusion rates in the irradiated particles exposed for 400 h. Planned STEM analysis will supplement the current observations and contribute to a more comprehensive understanding of the different oxidation responses observed over the range of exposure times used in this study.

2.1.3.3 Summary

An oxidation experiment was performed to understand the response of irradiated and unirradiated burn back TRISO particles (i.e., with the OPyC layer removed) under oxidizing environments. Analysis reported for the 1400°C, 50–400 h conditions showed a variation in failure fraction between the two particle types with an increase in failure at 400 h for the irradiated condition. This response was like that observed in historic oxidation tests of irradiated TRISO particles that still had the OPyC coating in place (Moormann 2011; IAEA 1997). Exploring burn back particles provided an opportunity to directly understand the impact of irradiation on oxidation kinetics. The parabolic rate constants fitted to the measured data were on the order of those reported for TRISO fuel particles, which provides confidence in the approach. Clear structural variations were observed between oxides formed on the SiC surfaces of irradiated and unirradiated particles that supported the difference in oxidation rate constants measured over the range of 50–200 h. Beyond 200 h, a deviation from the parabolic behavior was observed which was not unexpected and suggests parabolic models cannot be used to predict long term oxide growth.

For More Information:
John D. Stempien (john.stempien@inl.gov)
John D. Hunn (hunnjd@ornl.gov)
Tyler J. Gerczak (gerczaktj@ornl.gov)
Grant W. Helreich (helmreichgw@ornl.gov)

2.2 High-Temperature Materials

This quarter, INL staff continued to support ASME BPVC Section III, Division 5 committee activities. This support included attending and participating in various committee meetings held as part of the July Code Week which was held virtually. INL staff are chair and secretary for several of these committees. Updates on INL activities are provided at these meetings. This includes an update to the Allowable Stress Criteria committee regarding work being conducted to identify an improved filler metal for Alloy 800H. In addition to attending committee meetings that occur during Code Week, an INL staff member has been participating in the PM HIP process group which meets separate from Code Week. This process group reports to Section III, Division 1 Advanced Manufacturing Task Group. In addition to Code Week, INL staff attended the EPRI-NEI Advanced Reactor Materials Development workshop, the GAIN-EPRI-NEI Advanced Methods for Manufacturing Qualification Workshop, and the NRC Standards Forum. At the NRC Standards Forum, an INL staff member presented on the “Qualification of High Temperature Materials and Their Incorporation into ASME Section III, Division 5.”

A total of five Alloy 617 notched creep-rupture tests continued to be sustained this quarter. Both U- and V-notch specimen geometries are being explored. The purpose of these tests is to investigate the impact of geometric discontinuities and multiaxial stress states on creep-rupture behavior. This testing is needed to address NRC concerns that are beyond the scope of the ASME BPVC. A small-radius base-metal V-notch specimen ruptured this quarter. This specimen was tested at 900°C with an initial applied stress of 28 MPa. The purpose of this test was to understand the impact of a multiaxial stress state at test conditions that result in an intermediate creep-rupture life (approximately 12,000 to 16,000 hours). Next quarter, the data from this test will be analyzed and the microstructure of the unruptured notch will be characterized.

Work to revivify the testing capabilities necessary to investigate the impact of environment on fatigue and crack growth is ongoing. This quarter, machining of the Alloy 617 compact tension specimens was completed. The specimens were inspected so that they could be green tagged as quality level three. During this inspection, minor discrepancies between the engineering drawing and the specimens were noted and promptly rectified. Next quarter, efforts will continue to verify the test setup.

Work has been ongoing to identify a filler metal for Alloy 800H weldments with improved stress rupture factor (SRF) values compared to the SRF values for the filler metals qualified in Section III, Division 5 of the ASME BPVC for Alloy 800H weldments. An overmatched filler metal, Alloy 617, was investigated. Preliminary results do not indicate that Alloy 800H weldments with Alloy 617 filler metal will have significantly improved SRF values. Alloy 800H weldments with UTP A 2133 Mn filler metal will now be investigated. This filler metal was selected because it is currently being used by the European syngas industry because of its matching properties compared to Alloy 800H. A report, “Assessment of overmatch filler (Alloy 617) to improve Alloy 800H stress rupture factors,” was finalized on these findings (Rupp, 2021). This report was the deliverable for milestone M3AT-21IN060405. In addition to completing the milestone this quarter, two subcontracts were established. One subcontract is with the Materials and Corrosion Know-How B.V. The purpose of this subcontract is to leverage a consultant’s industry experience with UTP A 2133 Mn. The other subcontract is with Flatirons Metallurgical Consulting. This consultant has significant industry experience with welding. Alloy 800H plates were prepared for welding this quarter. Automated gas tungsten arc welding of Alloy 800H with UTP A 2133 Mn filler metal will begin next quarter.

Section III, Division 5 of the ASME BPVC specifies a temperature- and time-dependent allowable stress, S_t. This stress is defined as the lesser of three criteria. These criteria involve the stress to obtain 1% strain, to cause the onset of tertiary creep, and to cause rupture. The intent of the tertiary creep criterion was to slightly adjust without severely controlling the allowable stress. However, the contrary was observed during attempts to extend the qualified design lives of type 304 and 316 stainless steel and Alloy 800H. Consequently, the inclusion of the onset of tertiary creep criterion was evaluated. The result was the recommendation that an alloy specific ratio between the onset of tertiary creep and rupture be used. This significantly increases the amount of data taken under consideration when determining the stress to cause the onset of tertiary creep. These findings were summarized in the report titled “Recommendation for Limiting Conditions for ASME BPVC Section III Division 5 Allowable Stress Criteria” which was finalized this quarter (McMurtrey and Wright, 2021). This report was the deliverable for milestone M4AT-21IN0604021. The ballot to extend the life of type 304 and 316 stainless steel continues to progress through the various ASME BPVC committees.

Historically, creep and fatigue interaction evaluation involved the separate calculation of the creep and fatigue damage in a creep-fatigue test. The damages are then plotted on the damage diagram (D-diagram) to set the limitations defined by the allowable creep-fatigue damage envelope. This D-diagram approach has significant limitations and results in overly conservative design factors. These issues resulted in the development of the simplified model test (SMT), which eliminates the need for the D-diagram. The SMT approach defines elastic follow-up factor accounting for the stress redistribution when strain is confined which is observed in actual components experiencing creep degradation (Wang et al., 2019). Single bar SMT (SB-SMT) testing using software controls is being conducted to validate the method and compare to the original SMT testing that used hardware controls, as well as expanding on the SMT testing matrix. This SMT testing data is crucial for the development of an ASTM standard on SB-SMT testing. A critical difference between the testing being conducted with software controls in comparison to hardware-controlled testing is that the use of software rather than hardware to control the feedback. This significantly simplifies the test setup and makes the test method more practical for others conducting creep-fatigue interaction testing. This quarter a postdoctoral researcher started at INL who will conduct work in this area. The researcher is in the process familiarizing himself with this testing by reviewing literature and previous tests conducted at INL. A test matrix has been developed and SB-SMT testing at INL will resume next quarter.

In addition to the activities and work discussed in the previous paragraphs, planning for fiscal year 2022 was also carried out this quarter. Work packages were developed for operating under continuing resolution. The work packages were uploaded to PICs.

For More Information:

Sam Sham	*(tingleung.sham@inl.gov)*
Michael McMurtrey	*(michael.mcmurtrey@inl.gov)*
Joseph L. Bass	*(*joseph.bass@inl.gov*)*
Ryann Rupp	*(ryann.rupp@inl.gov)*

2.3 Graphite Development and Qualification

2.3.1 Irradiation Experiments – Graphite

Transfer of selected AGC-4 samples from HFEF to MFC AL for gamma spectroscopy evaluation of potential dose or contamination issues was completed in July. Subsequent gamma spectroscopy on selected AGC-4 samples at MFC AL was completed in August and found no aberrant isotopic content. Provisions were made for transfer of selected AGC-4 samples from MFC AL to IRC C19 Carbon Characterization Laboratory in September. However, shipment has been delayed pending resolution of newly raised questions from radiological controls personnel.

2.3.2 Materials: Graphite

2.3.2.1 Graphite Modeling

2.3.2.1.1 Assessment of an Oxidized Graphite Component

According to Section III Division 5 of the ASME BPCV, the full assessment of an oxidized graphite component is part of the design by analysis assessment methodology. In this methodology, a designer computes a probability of failure from the internal stresses in a component and the graphite's Weibull distribution of strength. Simulations were run using computed stresses in an oxidized graphite component to investigate failure calculation for the degraded component. This effort helps highlight areas in the code which maybe ambiguous or need additional attention. The initial work, discussed below, shows that graphite with degradation gradients is not easily handled by the full assessment.

The following example attempts to assess an oxidized graphite component using the full assessment described in the ASME code. As a problem setup, a block of graphite is exposed to oxygen on the right hand, as shown in Figure 13.

Figure 13. Oxidation example problem set up.

Oxidation simulations were run at two temperature, 825 K and 950 K, for a total mass loss of ten percent. This produced two distinct oxidation profiles, which are shown in Figure 14.

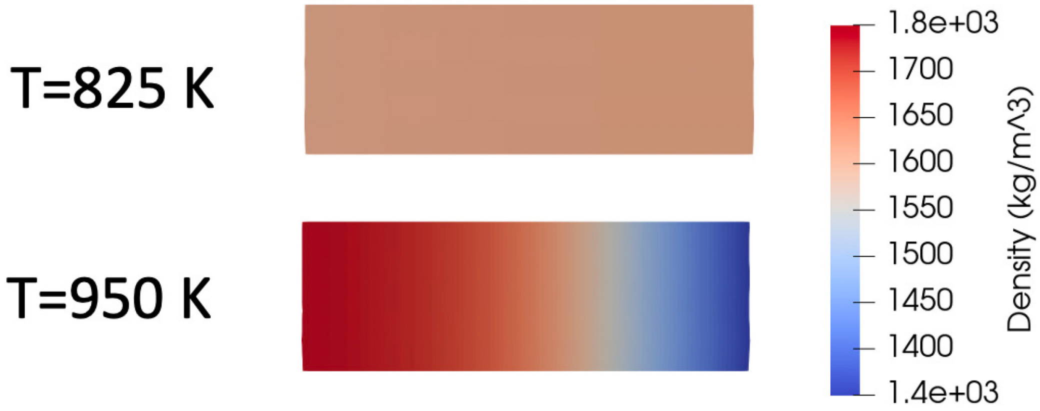

Figure 14. Density profiles in IG-110 oxidized at 825 K and 950 K to ten percent mass loss.

For this very simple example, each block is assumed to experience an evenly distributed 5 MPa stress. Now, with the oxidation degradation and stress profile known, implementation of the full assessment is attempted under the ASME code rules. HHA-3141 stipulates that material oxidized to greater than thirty percent mass loss or more than fifty percent strength loss should not be credited in the evaluation. This will remove the right portion of the graphite block oxidized at 950 K from the analysis, because that material will have more than fifty percent strength loss. From a designer's standpoint, a structural analysis should be performed at this point to determine stresses in the reduced block, but for simplicity we will maintain the 5 MPa. The next step in the full assessment is to use a Weibull distribution of strengths alongside the stresses to compute the probability of failure (POF). This poses a problem. Which Weibull distribution should be used? HHA-II-3200 designates how to compute the required Weibull parameters, but it implicitly assumes that the data set matches the strength properties of the component. This is simple enough if the component has homogenous properties (oxidation damage).

All that needs to be done is homogenously oxidize specimens and determine the strength loss. Although, for the case where there is a gradient, like the block oxidized at 950 K, it would be a herculean task to attempt to determine profile dependent Weibull parameters. How to handle strength gradients in the graphite remains an open question. One possibility, explored below, is instead of using a single set of Weibull parameters, use oxidation damage (density) dependent Weibull parameters.

If the full assessment POF calculation was altered in the following way

$$X_i = \left(\frac{\sigma_{vi} - S_0'}{S_{c095\%} - S_0'}\right)^{m_{095\%}} \quad \rightarrow \quad X_i = \left(\frac{\sigma_{vi} - S_{0,i}'}{S_{c095\%,i} - S_{0,i}'}\right)^{m_{095\%,i}}$$

where the addition of the '*i*' subscript designates that the parameter is a function of the local properties, then all that would need to be known are the Weibull strength parameters for homogenously oxidized components. To finish the problem, we can assume the Weibull parameters shown in Table 12. and linearly interpolate for find intermediate values.

Table 12. Weibull strength parameters implemented in full assessment example problem.

	Scale	Shape
As Manufactured	23.26	11.51
5% mass loss	16.21	10.49
10 % mass loss	10.63	7.14

Following the rest of the steps in HHA-3217 as they are written, the POF for the block oxidized at 825 K is computed as 5.34e-6 and the POF of the block oxidized at 950 K as 4.71e-7. While the quantitative results of this example problem are not important, this problem does highlight some of the difficulties a designer may encounter when using the ASME code.

2.3.2.1.2 Effective Diffusivity Evolution in Graphite

Improvements were made to the graphite oxidation model by investigating the evolution of the effective diffusivity as a function of mass loss. The oxidation model which is used in this work tracks the chemical species concentrations with an effective diffusivity term. As the graphite is oxidized the effective diffusivity varies. In this model the effective diffusivity is computed as

$$D_{eff} = D_{min} + f(\rho)(D_{max} - D_{min})$$

where D_{eff} is the effective diffusivity, D_{min} is the diffusivity of unoxidized graphite, D_{max} is free gas diffusion, and $f(\rho)$ is a function which transitions the effective diffusivity between the min and max values. In this work we assume that

$$f(\rho) = \rho^n$$

where '*n'* is an unknown to be solved for. Previous experimental oxidation work performed at INL on samples with variable size and shape act as an ideal data set to optimize the '*n'* against. The optimized '*n'* value was found to be approximately one half. The plots which show the simulation fits using the optimized '*n'* value are in Figure 15.

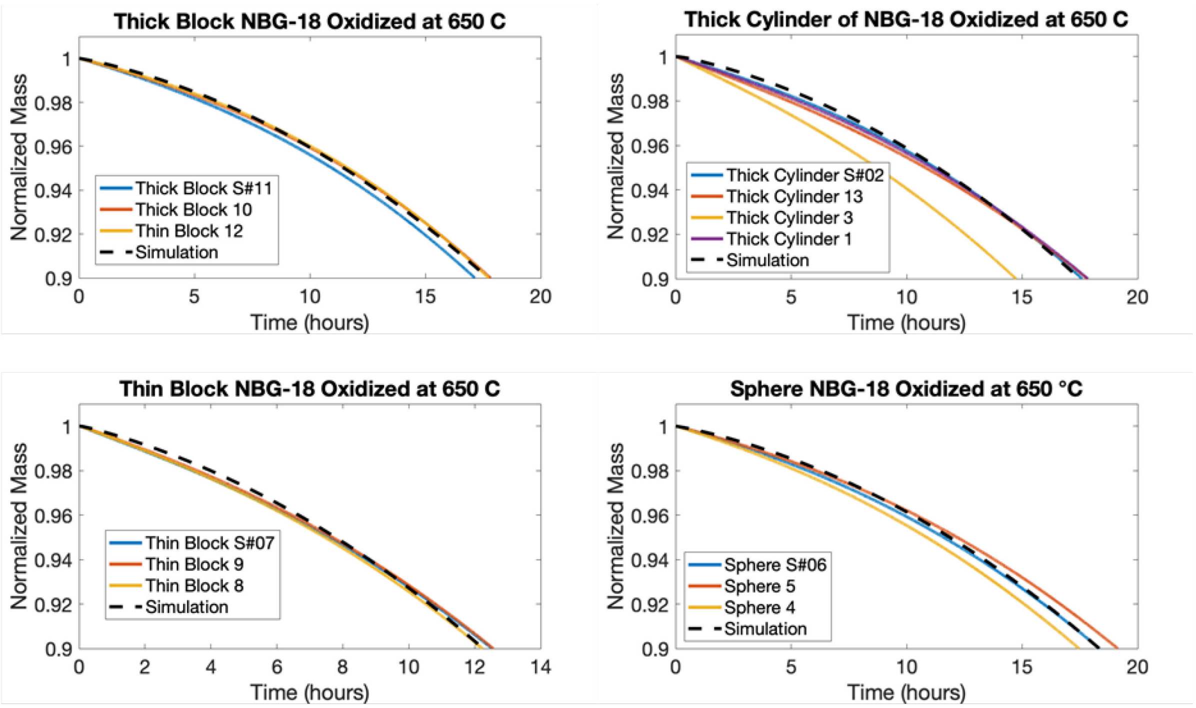

Figure 15. Simulated and experimental mass loss versus time trend for specimens of NBG-18 of various size and shape.

This ‘*n’* value is lower than what was expected theoretically, but experimental work on graphite diffusivity is being conducted at INL, and this work will help to further develop and improve this oxidation model.

2.3.2.1.3 Investigating the Oxidation Effects on IG-110 and NBG-18 Using Microstructural Based Models

The ORNL graphite research team has developed a methodology to process XCT data to create microstructural based models. In this research, the microstructural based models were used to assess the effective thermal conductivity and absolute permeability of graphite. Thermal conductivity and other mechanical properties decrease as a function of weight loss induced by oxidation. In this case, effective thermal conductivity calculations can help to assess how different types of oxidations would affect graphite. In similar fashion absolute permeability simulations are an indicator on the access of the oxidants to graphite components as well as the possible ingress of molten salts into the graphite open porosity. The proposed methodology will help to assess the performance of different graphite grades subjected to oxidation and in the future to other degradation mechanisms such as neutron irradiation effects. High resolution XCT scans of IG-110 and NBG-18 were segmented to differentiate between open porosity, close porosity and solid graphite (Figure 16).

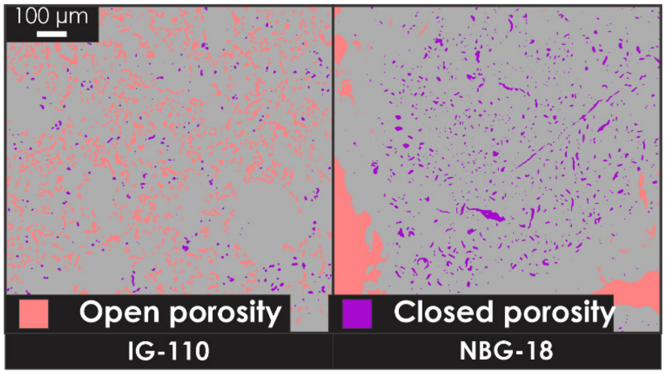

Figure 16. Cross section of segmentation showing open and closed porosity within graphite.

The methodology to estimate the effective thermal conductivity and absolute permeability was also adapted to assess how the listed properties change as a function of uniform oxidation. In this case the uniform oxidation was a product of pore dilation of the open porosity. A schematic that shows the dilation of a single voxel is shown in Figure 17. At each dilation step the voxels grew and connected with closed porosity; when open and closed porosity were interconnected the closed porosity became open porosity. In this way, gradual uniform oxidation can be simulated through the dilation of open porosity.

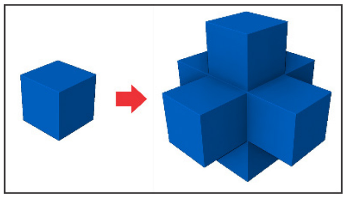

Figure 17. Schematic that shows the dilation of voxels. This process was used to simulate uniform oxidation.

The original and virtually oxidized segmentations were then used as inputs to estimate the effect of virtual oxidation on the thermal conductivity and permeability of the microstructures. Heat transient analysis simulations were used to estimate the effective properties whereas Stoke problem was solved to calculate the absolute permeability of the graphite microstructures. Figure 18 shows a diagram that summarizes the boundary conditions used to compute the effective properties of graphite.

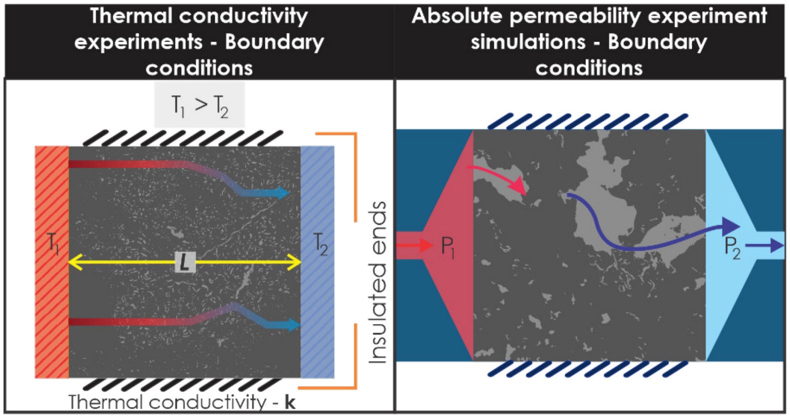

Figure 18. Boundary conditions to estimate the effective thermal conductivity and absolute permeability of graphite microstructures.

Segmentations and results of simulations for both IG-110 and NBG-18 are provided in Figure 19. These illustrations show how virtual oxidation reduces the thermal conductivity and increases the permeability of the grades. In case of the permeability simulations, the simulated fluid flows more freely in the oxidized microstructures than the original microstructure. In case of the thermal conductivity simulations the temperature distribution on the oxidized microstructures is less even and has larger temperature values at the edges of the geometry. From these results, it is also possible to conclude that uniform oxidation has a larger impact on the effective thermal properties of IG-110 than NBG-18. This is because the pore connectivity and content of open porosity is much larger in IG-110 than NBG-18.

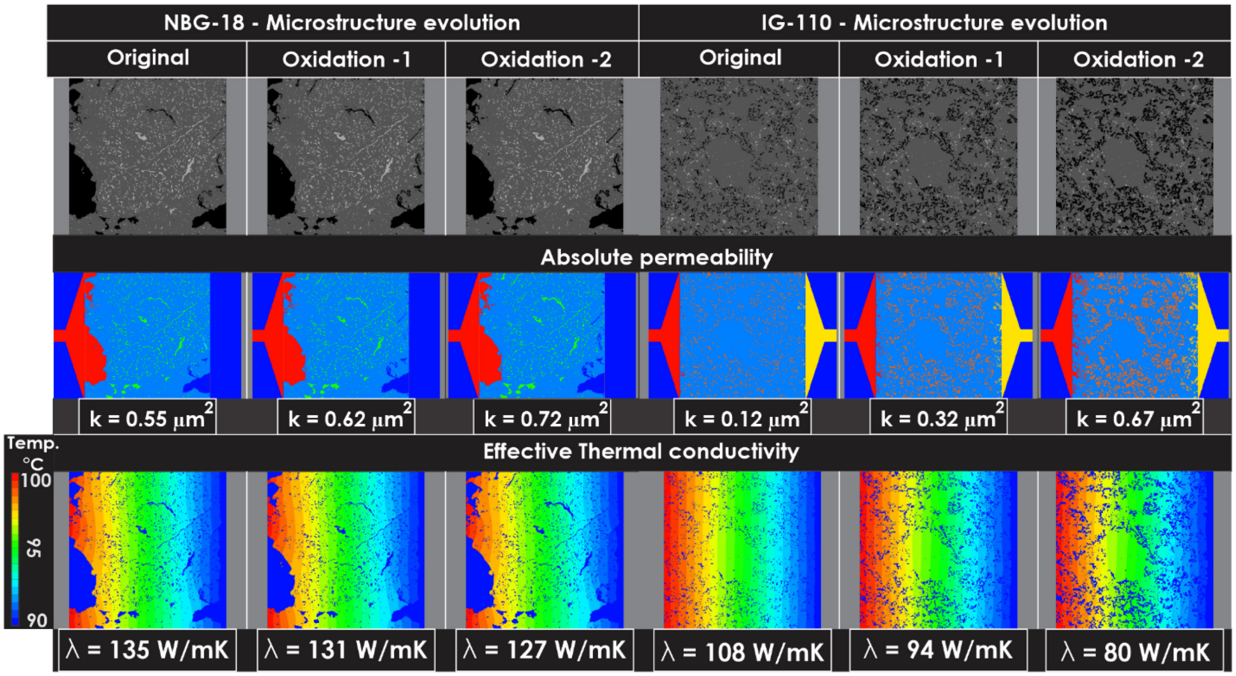

Figure 19. Microstructure segmentations, absolute permeability, and thermal conductivity simulations.

Further XCT characterization and microstructural based models will be performed in real uniformly oxidized samples. The pore morphology (pore shape and pore connectivity) and effective properties will be compared to assess the efficacy of virtually oxidized microstructures.

2.3.2.2 Microscopic Response of Thermally Annealed Graphite

The draft of a paper titled “Transmission Electron Microscopy Analysis and The Microscopic Response of Thermally Annealed Nuclear Graphite” has been developed for submission to *Journal of Nuclear Materials*. The key findings in this research show fullerene-like defect development due solely to thermal annealing. Consequently, such defects are conjectured to directly contribute to non-recoverable physical property change which has previously been observed in irradiated nuclear graphites (Figure 20).

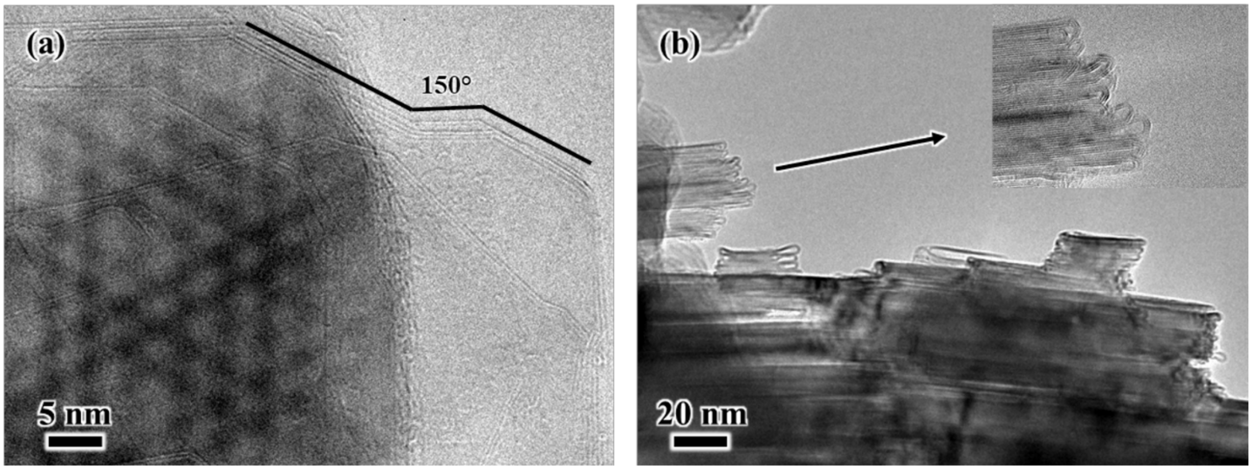

Figure 20. (a) high-resolution transmission electron microscopy (HRTEM) image along the c-axis of IG-110 prepared to electron transparency via oxidation prior to thermal annealing at 2500°C for 20 hrs. The moiré pattern is further evidence of rotational disorder amongst basal planes. Also shown in (a) is the preferential curling of basal planes edges along alternating crystallographic edges (the reference lines are drawn at 150°). (b) shows an HRTEM perpendicular to the c-axis where all edges of crystallites show a fullerene-like rearrangement.

2.3.2.3 MacroRaman Spectrometry

2.3.2.3.1 MacroRaman Upgrade

The upgrade of macroRaman spectroscopy is completed. The Raman system now can function under dual laser wavelengths (532 & 325 nm). The expanded capability can enable researchers to look into more defected microstructures in graphite.

Additional examination of experimental signal indicates that the result suffered from noises due to excitation of air molecules in the light path (Figure 21). A purging system is planned to remove the air molecules in the system to improve signal-to-noise ratio.

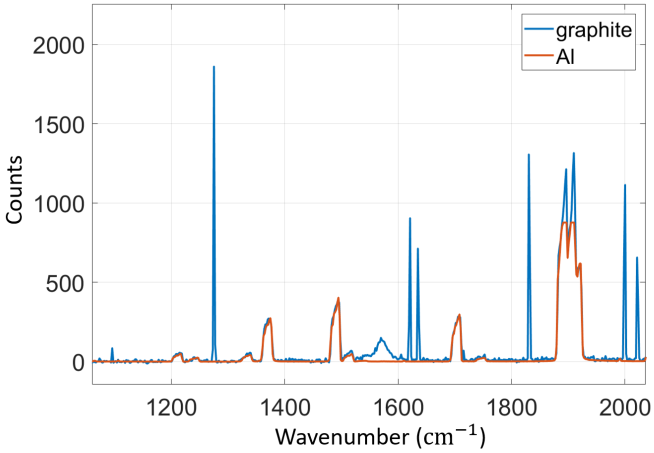

Figure 21. Example result of Raman spectra using macroRaman system at 325 nm.

2.3.2.3.2 Impact of Preparation Methods on Raman Spectrum

The laser light only penetrates a very thin layer (~ 10 nm) on graphite and serves as a surface characterization technique. In order to ensure that the properties measured at surface is representative of bulk properties, a comparison study is conducted. The Raman spectra of four differently prepared surfaces were measured using both micro and macroRaman spectroscopy.

Four IG-110 graphite samples were prepared with different surface preparation methods. Two samples are as machined and have different morphologies, one sample is polished, and one with fractured surface. The images of these surfaces are presented in Figure 22. The fractured surface is assumed to have the same microstructure as bulk graphite and serves as the reference sample.

Figure 22. Images of the surfaces of four graphite samples prepared in different methods.

The Raman spectra from macro and microRaman spectroscopies are presented in Figure 23 and Figure 24. The Raman spectra from both methods agree. The polished and shiny surfaces display large D peaks (~1350 cm^{-1}) while the D peaks on fractured and rough surfaces are small.

The polished and shiny surfaces display the largest D peaks, indicating that these surfaces possess more damaged microstructures compared to the bulk graphite revealed by fractured surface. In addition, large variation in the results of shiny surface is observed. The Raman spectra from rough surface are similar to those from fractured surface and can be used to investigate the changes of bulk properties.

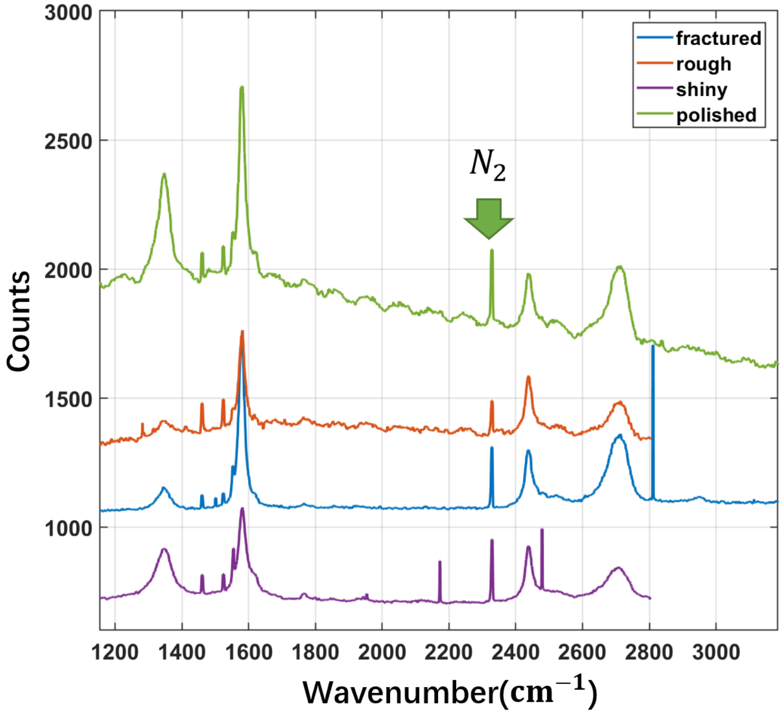

Figure 23. Raman spectra on four graphite surfaces from macroRaman spectroscopy.

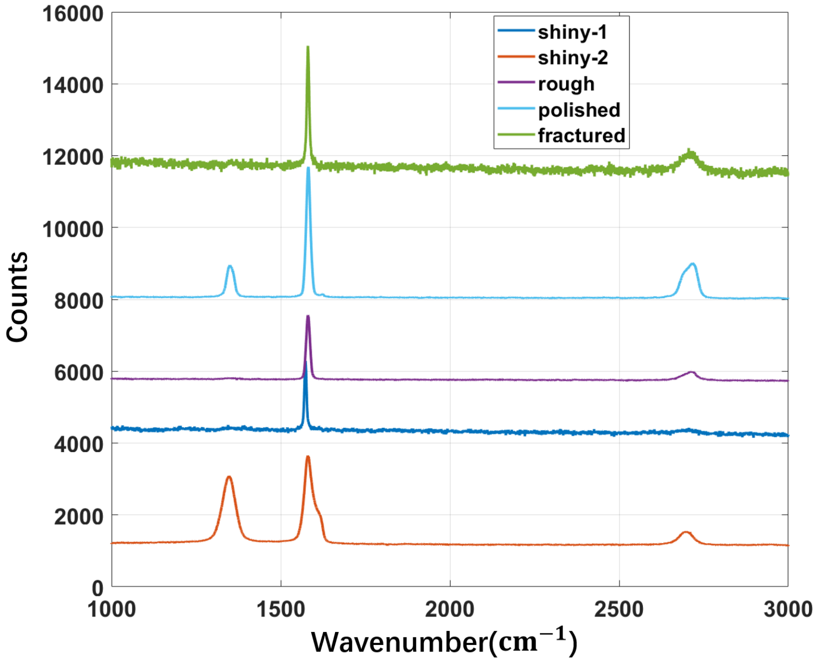

Figure 24. Raman spectra on four graphite surfaces from microRaman spectroscopy.

2.3.2.4 Compressive Testing of Salt-exposed Graphite Samples

ORNL initiated some scoping studies to understand the effect of salt intrusion on the mechanical properties of graphites. Room temperature compressive testing was undertaken on cylindrical samples of three grades of fine grade graphite, to evaluate the effect of FLiNaK molten salt infiltration. Samples were exposed to FliNak for 12 hours at 750 °C at 101 psig. For each grade, a total of six control samples and four infiltrated samples were tested in compression following ASTM C695. The infiltrated samples were cleaned before testing, using a combination of boiling water, sonication in deionized water, and vacuum drying, although over 50% of the salt remained in the graphite after cleaning.

The bar chart in Figure 25 illustrates the D_0 parameter following infiltration and then following cleaning for the three grades. D_0 is defined as the ratio of actual salt uptake to the amount of salt that would fill the open pore volume. A ratio of greater than 1 indicates that closed pores were accessed due to the high infiltration pressure. Due to the relatively low solubility of the salt components in water, only a portion of the salt was removed.

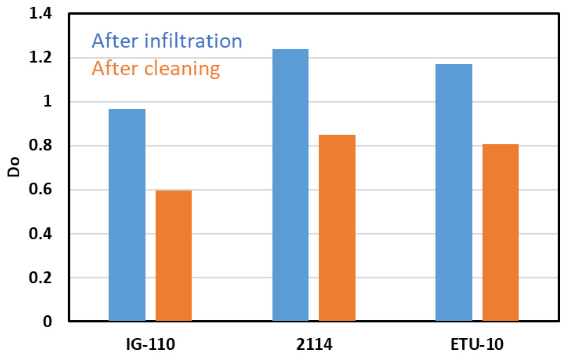

Figure 25. D_0 parameter calculated after intrusion testing and after cleaning cycles aimed at removing the salt intruded.

The nominal diameter of the samples was 10 mm and the height was 20 mm, meeting the aspect ratio requirements. One finding was that the average compressive strength (at room temperature) was slightly increased by infiltration, although the mechanism is not yet clarified, and more work is being performed. Figure 26 shows dot plots of the compressive strengths for each graphite grade. Salt remaining in the pores and cracks in the sample certainly contributed to higher strengths. However, note that Mersen 2114 experienced an almost 10% strength increase, while ETU-10 barely had an increase, while their D_0 value post cleaning were very similar.

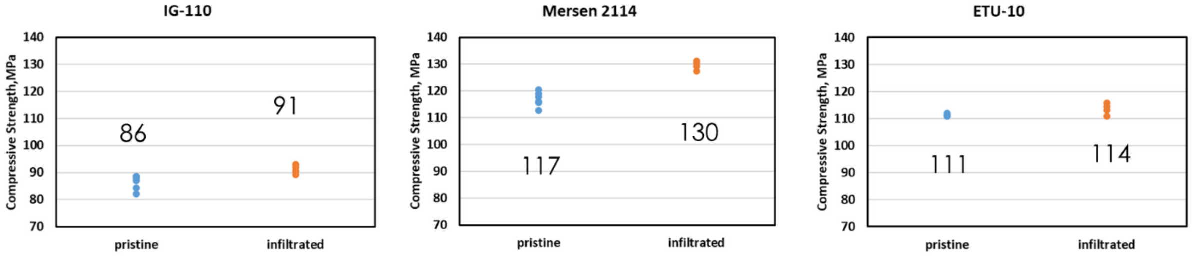

Figure 26. Room temperature compressive strength for pristine and salt-infiltrated samples for three fine grain graphites.

The stress-strain curve shows a systematic increase in stress at strain levels near the maximum strain for all the grades. An example for the Mersen 2114 samples is shown in Figure 27. Additional characterization work will be performed to better understand the findings.

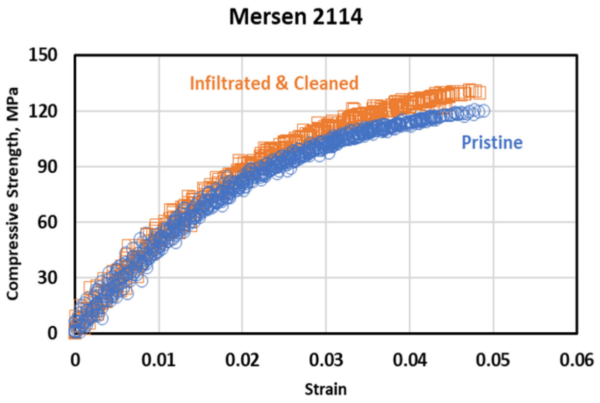

Figure 27. Typical strength-strain curve for graphite grade Mersen 2114.

2.3.3 Collaborations and Licensing: Graphite

2.3.3.1 ASME BPVC.III.5 Code Status

Finalizing its review, the U.S. NRC released the draft documents, DG-1380 and NUREG-2245 for public review in August 2021. It endorsed ASME BPVC III.5 with exceptions and limitations. Several paragraphs under Subsection HA (General Requirements) Subpart B (Graphite and Composite Materials) included exceptions to reference to Subsection NCA instead. Partly this is because there was an effort during 2019 through 2020 to integrate the 2017 edition Subsection HAB with the Subsection NCA. Several of these exceptions and limitations are now adopted in the 2021 edition.

Two specific limitations mentioned were the use of certified engineers who also need to be registered professional engineers and the use of ISO/IEC 17025 2017 edition (as oppose to the 2005 edition). It also identified that numerical parameter limits defined for weight loss, cohesive life, gas flow velocity and allowable repair depth do not have a basis for generical application. These parameters need to be assessed and either revised with a technical basis or not specifically called out. In addition, it mentions to endorse Mandatory HHA-III-4200 with the exception that irradiated and oxidized material property data used for populating the Material Data Sheet, needs to come from testing performed on material representative of the production billet. The review excluded later code editions which included the composite components and was therefore silent on Subsection HHB. The review was not performed outside the scope of Div. 5 and therefore excluded scope referencing Section XI on Inservice Inspections.

Several of the limitations and exceptions mentioned are already in process or have been addressed through records 20-142 (the revise Section III, Division 5, Subsection HA, Subpart B to align with changes introduced into Section III, Subsection NCA in the 2019 Edition), 20-1306 (modification of HHA-3143 on abrasion and erosion) and 21-1392 (modifications related to graphite oxidation).

The third 2021 quarterly meeting of the ASME NDM WG was held virtually on July 27th, 2021, maintaining community interest and participation with at least 27 attendees. The committee was well represented with a good spread between HTR vendors, material scientists and engineers, regulator, individuals and international participants.

Three of the six task groups identified as optimization areas required for the code are making headway for implementation, on aspects concerning Weibull and stress calculation formulas, graphite oxidation and damage tolerance of the graphite core.

The task group on all aspects Weibull had their first record (#20-1308), to modify the Weibull analysis nomenclature, pivotal quantity figures and parameter definitions within subsection HHA paragraphs HHA-II-3100 and HHA-II-3300. The record was approved by the nonmetallic design and materials working group. It will next be presented at the subgroup committees. The next focus will be to correct the three parameter Weibull applications as defined under HHA-II-3200 and HHA-II-3217.

The task group addressing open questions on oxidation matters have their first record (#21-1392), addressing the obvious changes as well as new proposed limits (HHA-3141), passed the working group ballot. These changes will now be proposed to the subgroup committees.

The task group addressing parts of the code as it relates to damage tolerance of the graphite core, has the first draft whitepaper "Damage Tolerance in Graphite Components" reviewed by the working group and code changes are being reviewed for implementation. One significant change will be the extension of the code to expand the rules under Section XI (Inservice Inspection), to include graphite and composite components.

In addition to the graphite task group activities, efforts have been focused on the review of the ceramic composite rules under Subsection HHB. Records #21-728 on HHB corrections and #20-1307 on C-C composites have progressed passing approval of the working group. There is also initiative to address community questions on material qualification processes and its objective is also to work with the community to develop a benchmark study to support the technical basis of the design rules as well as perform review of paragraph HHB-3000.

2.3.3.2 Graphite Strength with Oxidative Mass Loss under ASME BPVC.III.5

ASME BPVC Section III Division 5 Subdivision HA (Nuclear Graphite) has two important recommendations regarding stress evaluation of oxidized graphite components:

- The strength (both tensile and compressive) decreases as a function of weight loss as shown in Figures HHA-3141-1 and HHA-3141-2 (or alternatively from the Material Data Sheet HHA-2200). The stress evaluation shall be made according to this relation. The region where strength decreases to less than 50% shall not be credited in the stress evaluation (HHA-3141-b).
- The region where the amount of weight loss exceeds 30% shall be regarded as completely removed from the structure for both oxidation and strength calculations (HHA-3141-c).

Two important questions were raised by the above statements:

1. Considering that Figure HHA-3141-1 refers to classes IIHP and INHP (isomolded isotropic and near isotropic high purity) graphites and Figure HHA-3141-2 refers to classes EIHP and ENHP (extruded isotropic and near isotropic high purity) and classes MIHP and MNHP (molded isotropic and near isotropic high purity) graphites, are they conservative enough and supported by credible experimental data?
2. Are the above numbers (30 % weight loss and 50 % strength loss) correlated, and supported by reliable experimental results?

In response to the **first question**, the original source of the two figures was found in a Japanese language document used for the design of HTTR reactor at the Orai Research Establishment.[a] The same figures were later reproduced in a paper published in 2004.[b] According to this paper, data were obtained from measurements by Japanese researchers on uniformly oxidized graphite specimens. From this publication's references it was found that Figure HHA-3141-1 is based on compressive and tensile strength data for graphite IG-11 reported in 1984 by Japanese researchers.[c] On the other hand, Figure HHA-3141-2 is based on compressive and tensile strength data for uniformly oxidized graphite PGX reported by Brookhaven National Laboratory[d] and by General Atomics.[e]

As Figure 28 shows, the two sets of results are blatantly different: at equal mass loss levels, strength loss decays faster for PGX (half of original strength at 6 % mass loss, as in Figure HHA-3141-2) than for IG-110 (half of original strength at 10 % mass loss, as in Figure HHA-3141-1). These graphs in Figure 28 (minus the data points) were reproduced in ASME code as HHA-3141-1 and HHA-3141-2.[b] Why this difference? Are these data credible? Is the more conservative behavior in Figure 29 the trend that should be recommended by the ASME code?

---

[a] "Graphite Structural Design Code for the High Temperature Engineering Test Reactor", JAERI-M 89-006, January 13, 1989.

[b] M. Ishihara, J Sunita, I Shibata, T Iyoku, T Oku, "Principle design data of graphite components", Nuclear Engineering and Design 213 (2004) 251-260

[c] S. Yoda, M, Eto, T. Oku, T Sogabe, "Effect of oxidation on tensile and compressive deformation behavior for nuclear-grade isotropic graphite" Intern. Carbon Conf. 84, Bordeaux, France.

[d] M Eto, F B Growcock, "Effect of prestress and stress on the strength and oxidation rate of nuclear graphite", NUREG/CR-2316, 1981.

[e] R J Price, L A Beaven, "Strength of nonuniformly oxidized PGX graphite" GA-A16720, 1981

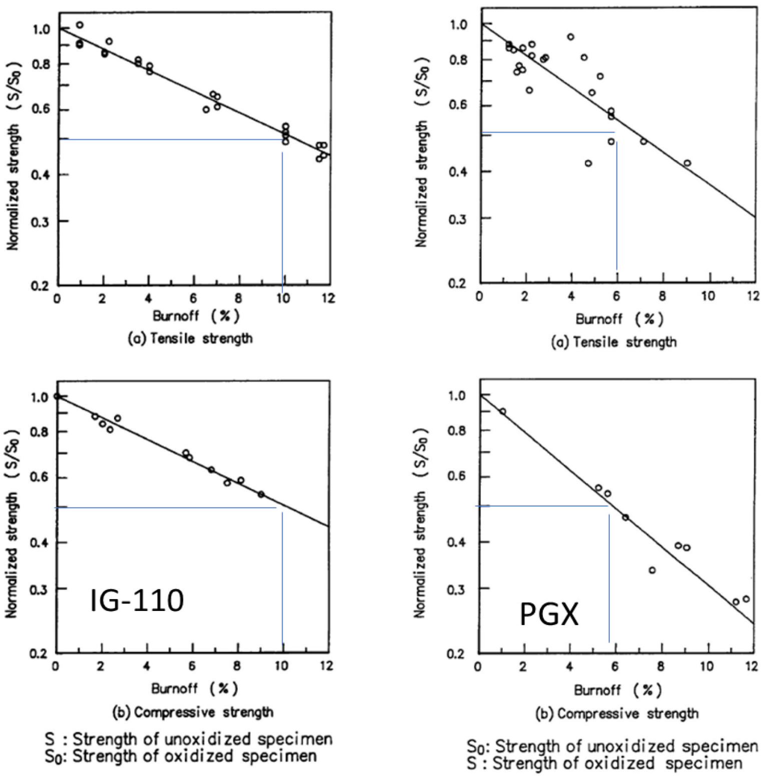

Figure 28. Mass loss (burnoff %) versus Normalized Strength (compressive and tensile) for uniformly oxidized specimens of isotropic graphite IG-110 and extruded graphite PGX (with high level of catalytic impurities.

Searching the original literature sources, graphite PGX was found to have had very high ash content (6400 ppm) including metals known as catalysts for carbon oxidation (Fe - 3000 ppm; Ca – 250 ppm, Cu – 140 ppm, Ba – 100 ppm). This high impurity content explains the difference between oxidation behavior of PGX compared with IG-11 and IG-110.[f] Therefore, Figure HHA-3141-2, showing oxidation data for impure PGX graphite is not representative for modern high purity nuclear graphite grades and should be dropped from the future editions of the ASME code.

---

[f] R J Price, L A Beaven, “Strength of nonuniformly oxidized PGX graphite” GA-A16720, 1981

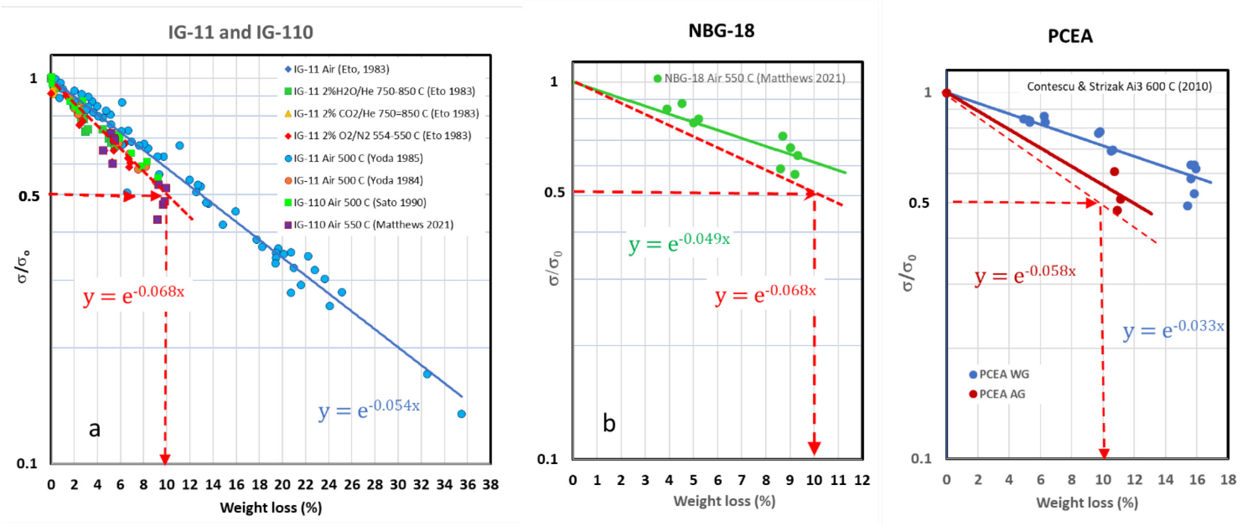

Figure 29. Left: Literature data on compressive strength degradation of uniformly oxidized IG-11 and IG-110 graphites in various oxidizing atmospheres (air, H_2O/He, CO_2/He). Center: Compressive strength data for graphite NBG-18. Right: Compressive strength data for graphite PCEA (two orientations). Most data show milder strength degradation (lower exponent) than the "rule of thumb" prediction (i.e. 10 % weight loss causing 50 % loss of strength, red broken lines).

On the other hand, data on IG-110 were confirmed by other reports which explored a broader mass loss range and various oxidants, including not only air but also H_2O/He and CO_2/He mixtures.[g,h] According to these reports, the degradation of graphite properties (compressive and tensile strength, bending strength, Young's modulus) corelates with the change of mass loss (or density) and reflects the development of porosity. Numerous reports have shown that, for **uniformly oxidized** graphite, the following empirical relationship, known as the Knudsen's formula,[i] applies. Later, Knudsen's relationship has found theoretical justification:[j]

$$\frac{\sigma}{\sigma_0} = \left(\frac{\rho}{\rho_0}\right)^{-n}$$

which is equivalent to:

$$\log\left(\frac{\sigma}{\sigma_0}\right) = -n \times WL$$

Here σ_0 and σ are the strength values of unoxidized and uniformly oxidized specimens, ρ_0 and ρ are the corresponding densities, and *WL* is the percentual weight loss. The exponent *n* was found to vary between 4.3 and 6.2 for IG-110. The higher the value of *n*, the more aggressive is the strength loss. Some researchers have found that, in general, 10 % mass loss in uniformly oxidized graphite corresponds roughly to 50 % (or less) strength loss and referred to it as a "rule of thumb" for property degradation in uniformly oxidized graphite.

---

[g] S Yoda, M Eto, K Tanaka, T Oku, "Effects of oxidation on compressive deformation behavior of nuclear grade graphite", Carbon 23 (1985) 33-38.

[h] M Eto, T Kurosawa, S Nomura, H Imai, "Evaluation of the oxidation behavior and strength of the graphite components in the VHTR (I) Normal Operation Condition", JAERI-M 87-056 (1987).

[i] F P Knudsen, Dependence of mechanical strength of brittle polycrystalline specimens on porosity and grain size, Journal of American Ceramic Society 42 (1959) 376-387.

[j] R W Rice, Comparison of physical property-porosity behavior with minimum solid area models Journal of Materials Science 31 (1996)1509-1528.

Related to the **second question**, Figure 29 shows plots of compressive strength vs. weight loss data extracted by digitalization from literature. Over a broad weight loss range, and for different selections of oxidizing atmospheres (air, H2O/He and CO2/He) the trends follow the Knudsen's relationship. The red broken lines correspond to the "rule of thumb" (exponent n = 6.8). With one exception, most data for IG-11 and IG-110 are linearized with lesser exponent values, meaning that their loss of strength is milder than what might be predicted by the "rule of thumb". Figure 29 shows recent data measured at INL for IG-110 graphite uniformly oxidized at 550 °C[k] and at ORNL for graphite PCEA with AG and WG directions.[l] With one exception, most data in Figure 29 show that the "rule of thumb" is the most conservative case for strength degradation of these uniformly oxidized graphites.

In conclusion, the Graphite Oxidation Task Group has the following recommendations for discussion and approval at the next meeting of the ASME Graphite WG (November 2nd, 2021):

1. Drop Figure HHA-3141-2 from the Code, because it is not representative for the behavior of high purity nuclear graphite, as defined by ASTM D7219-19 ("Standard Specification for Isotropic and Near-isotropic Nuclear Graphites")[m].
2. Move Figure 3141-1 to the Non-Mandatory Annex section and introduce it as an example for the behavior of uniformly oxidized graphite IG-110, supported by historic data.
3. Drop "30 % weight loss" and replace with "10 % weight loss" in HHA-3141-c. Based on the above examples, the "rule of thumb" referred in the literature is more conservative than actual experimental data, as could be found in the published literature at the time of this writing.
4. Specify in the Code that, rather than using Figure HHA-3141-1, the designer must determine the strength loss versus weight loss for each graphite grade used in the design (HHA-2200). Specify that properties testing must be done on uniformly oxidized specimens up to at least 10 % weight loss and reported in Material Data Sheet (HHA-2230).
5. Draft and publish White Paper(s) to clarify graphite-specific mechanisms of chronic and acute oxidation, development of non-uniform density profiles in oxidized layers, their relationship with degradation of mechanical properties, and provide literature examples of using graphite oxidation modeling for estimation of probable effects of graphite components oxidation within the qualification range defined by at HHA-2131 (Design Specification).

2.3.3.3 Conference Participation

Two significant events were held in September 2021. ASTM hosted virtually a symposium on graphite testing for nuclear applications. And the 21st INGSM 2021, was hosted virtually by North Carolina State University, Raleigh, NC, USA.

2.3.3.3.1 ASTM Symposium

An ASTM Symposium entitled 'STP1639 Graphite Testing for Nuclear Applications: The Validity and Extension of Test Methods for Material Exposed to Operating Reactor Environments' was successfully organized and delivered, taking place on September 23 & 24, 2021. Presentations from the USA, the UK and China covered (i) measurement strategy and characterization, molten salt reactors and oxidation and (ii) physical and mechanical property measurements.

---

[k] A C Matthews, J J Kane, W D Swank, W E Windes, "Nuclear graphite strength degradation under varying oxidizing conditions", Nuclear Engineering and Design 379 (2021) 111245.

[l] C I Contescu, J P Strizak, T R Guldan, T D Burchell, "Effect of air oxidation on pore structure development and mechanical properties of nuclear graphite", ORNL/TM-2010/197.

[m] ASTM D7219-19, "Standard Specification for Isotropic and Near-isotropic Nuclear Graphites", ASTM International, 100 Barr Harbor Drive, PO Box C700, West Conshohocken, PA 19428-2959, United States.

ART Program affiliates offered the following presentations and were active in nearly all the discussions throughout the ASTM Symposium:

- “A Microstructural Modeling Based Approach to Graphite Oxidation Beyond ASTM D7542”, by R. Paul, et al.
- “Evaluating the Effect of Molten Salt on Graphite Properties Gaps, Challenges and Opportunities”, by N. C. Gallego, et al.
- “Performance of Graphite Oxidation with Environment and Specimen Geometry”, by R. E. Smith and W. E. Windes.

The material presented will be published in a peer-reviewed ASTM publication in 2022.

2.3.3.3.2 INGSM

Graphite research sponsored by the ART Program was also well represented at INGSM 2021. In addition to making up more than 14 percent of the audience and moderating most of the sessions, ART Program participants offered the following presentations:

- “Graphite Oxidation in HTGRs: Addressing Information Gaps and Improving Design Rules for Graphite Components in ASME Code” by R. Paul, et al.
- “Recent Reviews, Development and Future Directions in the ASME Section III, Division 5 Code for Graphite and Composite Qualification and Certification”, by J. W. Geringer, et al.
- “Overview of ORNL’s Molten Salt Reactors Graphite Activities”, by N. C. Gallego, et al.
- “Neutron induced changes in properties and microstructure of glassy carbon”, by J. D. Arregui-Mena, et al.
- “Recent progress in the microstructural characterization and modeling of nuclear graphite”, by J. D. Arregui-Mena, et al.
- “Overview of DOE GSR Graphite Activities”, by W. E. Windes, et al.

For More Information:

William E. Windes	*(william.windes@inl.gov)*
Michael D. Davenport	*(michael.davenport@inl.gov)*
Rebecca E. Smith	*(rebecca.smith@inl.gov)*
Joseph L. Bass	*(joseph.bass@inl.gov)*
Philip L. Winston	*(philip.winston@inl.gov)*
Austin C. Matthews	*(austin.matthews@inl.gov)*
Andrea L. Mack	*(andrea.mack@inl.gov)*
Yuzhou Wang	*(yuzhou.wang@inl.gov)*
Steve Johns	*(stevejohns@u.boisestate.edu)*
Martin Metcalfe	*(martin.p.metcalfe@gmail.com)*
Cristian Contescu	*(contescuci@ornl.gov)*
J. Wilna Geringer	*(geringerjw@ornl.gov)*
Ryan Paul	*(paulrm@ornl.gov)*
David Arregui-Mena	*(arreguimenjd@ornl.gov)*
Nidia C. Gallego	*(gallegonc@ornl.gov)*

2.4 Design Methods and Validation

2.4.1 Severe Accident Heat-Removal Testing

Accomplishments on the NSTF program during the final quarter of FY21 included completion and submittal of two PICS:NE milestones; completion of the programs 71st data-quality matrix test, and start of the scheduled 4-month maintenance period.

A Level 2 milestone (M2AT-21AN0602012) on the Experimental activity and a Level 3 on the supporting Modeling activity were completed during the fourth quarter and submitted to PICS:NE. The Level 2 project deliverable, titled "Test report on Year 3 of water NSTF matrix testing program" was completed on schedule and submitted to PICS:NE. This milestone report provides a summary of FY21 testing on the water-based NSTF covering the two-phase parametric test series. The Level 3 milestone (M3AT-21AN0602014) deliverable, titled "Progress report on computational modeling of water NSTF", was completed on schedule and submitted to PICS:NE. This milestone report provides a summary of the computational modeling and analysis work performed in FY21.

DataQuality071, a matrix test within the Loss Coefficient parametric series, was conducted and successfully completed by the experimental team. This latest test case revisited the loss coefficient parametric series and continued the study of stability and performance with varying inlet restrictions. Portions of this test had been repeated during DataQuality064 and 067, with new levels of restriction explored in this latest case. This test was conducted at baseline conditions with continuous replenishment of boil-off condensate to achieve steady-state mode of flow operation. The operating window for active test operations (powered heaters) during DataQuality071 began at 19:00 on August 11, 2021 and spanned a period of 22 hours and 7 minutes. The onset of boiling occurred at approximately 12.5-hours into the test, and throttling began near the 15-hour mark. Following, 10 stages of inlet restriction were imposed on the operating test loop, Figure 30 . At Stage 1, the inlet valve was fully open with 100% available flow area. Following, step-wise reductions were made with the throttle area over the course of 10 stages, ending with the final stage allowing only 17% area for flow.

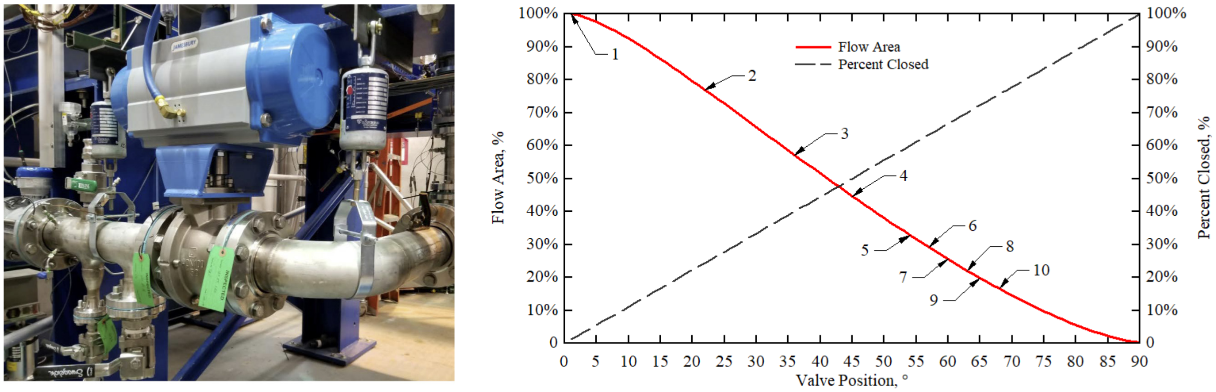

Figure 30: Inlet header throttle valve (left), Flow area vs Throttle position (right).

At each stage, the facility was allowed at least 20- minutes for stabilization of system flow rates, liquid temperatures, etc. Increments between stages were coarse at early portions, and more granular during later portions due to the non-linear relationship between valve angle and flow area. Early-stage flow restrictions initially resulted in flow stabilization, however as the area reduction progress they were followed by onset of unstable Type-II density wave oscillations at higher area reductions, Figure 31. At late stages of the test with high throttling, the low flow rates allowed sufficient power to enter the local fluid that the saturation temperatures could be reached even before rising in elevation through the chimney. The phenomena drove the onset of the parallel channel instability (PCI) mechanism, which drove out-of-phase voiding and independent flow excursions across the 8 parallel riser tubes. The PCI instability is a unique phenomenon that arise from coupled influences of flashing, boiling, and geysering.

The behavior can be chaotic in nature, with random flow reversals in individual channels a common occurrence. Elements of geysering were also evident, due to the stagnation of system flow, period of quiescence, and sudden eruption due to voiding.

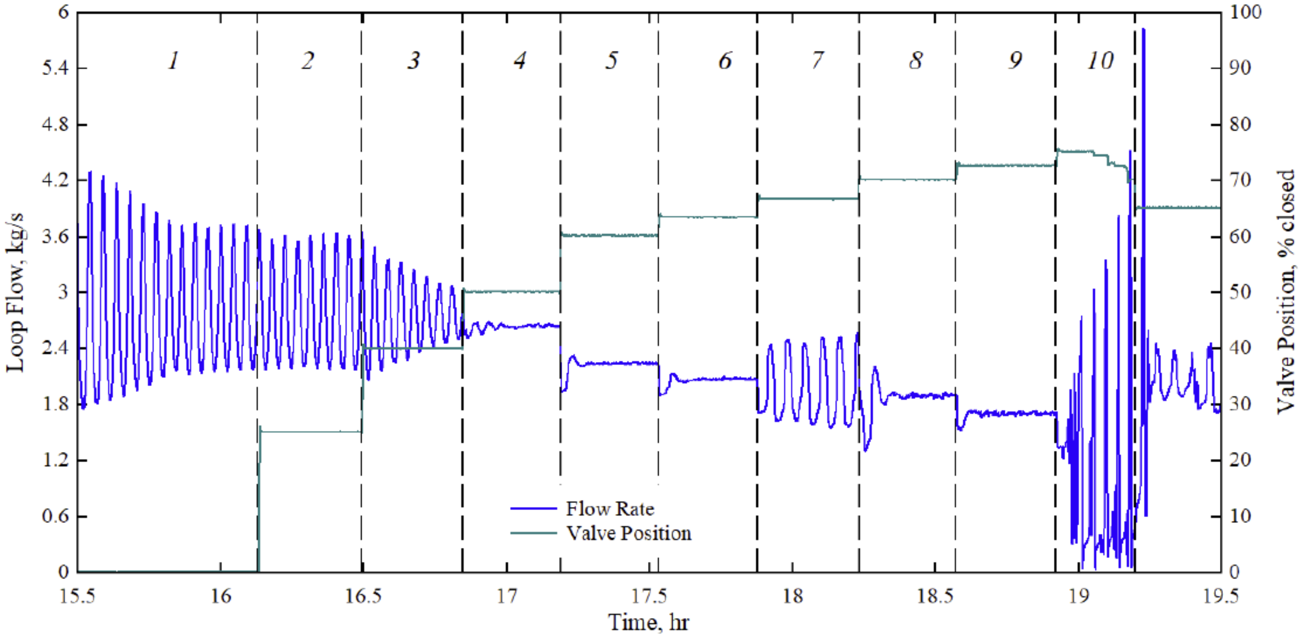

Figure 31: Stages of throttle valve position and resulting impact on system flow.

Planning and preparations for the upcoming shutdown period were completed, and the facility was placed into cold stand-by mode. The primary items planned for this maintenance period include inspection and emissivity measurement of the cavity, servicing of the R410a chiller, flushing of the network piping and water storage tanks, and repair of two erratic thermocouples on the heated panel. This maintenance period began in early September with draining of the loop inventory, de-energization of high voltage electric systems, and application of lockout/tagout on valves and power systems. Work then began with removal of the outer insulation panels to expose the electric heaters and allow access for repairs of the two faulted Guard zones. This work entailed significant use of the high-bay overhead crane, and required approximately 10 working days to complete. All heater insulation panels on the East (heated) wall, and half of the North and South (side walls) have been removed. Work then continued on accessing the 6N Guard heaters, which required removal of inner insulation and mounting hardware. Upon inspection, it was found that a portion of the heater element had burned out leaving a charred mark. The location of the burn point was immediately adjacent to a mounting stud, thus it is believed that the electrical insulator used to isolate the mounting hardware from the elements had failed and a short circuit was made between these two parts. Thus, the heater plate was then removed in it's entirely and replacement element installed, Figure 32. Currently, work is in progress on remounting the new element, installing the new interior insulation, and completing the electrical hookup of the power leads.

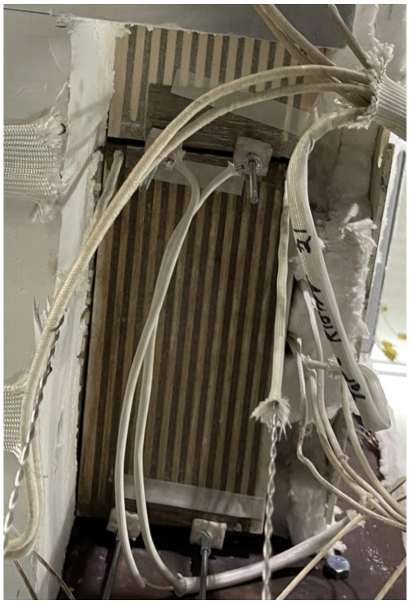

Figure 32: Exposed heater element, Guard 6N.

2.4.2 RELAP5-3D Code Qualification

During this quarter, the final document of the DOE milestone on the RELAP5-3D code qualification using HTTF data has been submitted on time and within budget. This milestone looked at test PG-27 conducted in the HTTF. The highlights of this study have already been summarized in the third quarter report INL/EXT-21-64809.

The HTTF benchmark effort has just been kicked off. Decision made so far include:

- Table 13. shows an overview of the HTTF test matrix that had been performed during 2019. It has been decided to focus for the benchmark on tests PG-26 (Depressurized Conduction Cooldown DCC), PG-27 (Pressurized Conduction Cooldown PCC) and PG-32 (Lower plenum mixing for CFD analysis).
- The benchmark will be presented to the Organisation for Economic Co-operation and Development / Nuclear Energy Agency for consideration to be included in their benchmark suite.

Table 13. HTTF Test Matrix 2019.

Test Number	Title	Date
OSU-HTTF-TEST-27	Low Power (<350kW) Complete Loss of Flow, 2 Heaters	May 24, 2019
OSU-HTTF-TEST-26	Low Power (<350kW) Double Ended Inlet-Outlet Crossover Duct Break, 2 Heaters	Jun 3, 2019
OSU-HTTF-TEST-35	Zero Power Crossover Duct Exchange Flow and Diffusion Test 1	Jun 4, 2019
OSU-HTTF-TEST-28	Low Power (<350kW) Lower Plenum Mixing Test	Jul 24, 2019
OSU-HTTF-TEST-29	Low Power (<350kW) Double Ended Inlet-Outlet Crossover Duct Break, Hybrid Heater	Jul 26, 2019
OSU-HTTF-TEST-34	Low Power (<350kW) Asymmetric Core Heatup Full Hybrid Heater	Aug 1, 2019
OSU-HTTF-TEST-32	Low Power (<350kW) Asymmetric Core Heatup	Aug 29, 2019
OSU-HTTF-TEST-30	Low Power (<350kW) Lower Plenum Mixing, Constant Temperature Test	Aug 30, 2019
OSU-HTTF-TEST-31	Low Power (<350kW) Pressure Vessel Bottom Break with Restored Forced Convection Cooling Test	Aug 31, 2019
OSU-HTTF-TEST-33	Zero Power Long Term Cooldown Test	Sep 4, 2019

For More Information:
Darius Lisowski (dlisowski@anl.gov)
Aaron Epiney (aaron.epiney@inl.gov)

3 90 DAY LOOK AHEAD

3.1 Fuels Development

- Complete LBL analysis of radially deconsolidated AGR-3/4 Compact 1-3 currently underway at ORNL.
- Initiate radial deconsolidation and LBL of AGR-3/4 Compact 10-2 at ORNL.
- Complete TEM examination of AGR-2 UCO Compact 5-4-2 particles from the 200 h and 400 h FITT oxidation tests at 1400°C.
- Complete SEM/FIB analysis of particles from AGR-2 UCO Compact 5-4-2 particles exposed to an oxidizing atmosphere in the ORNL FITT for 400 h at 1200°C.
- Complete a report for the Generation IV International Forum (GIF) to document the analyses at ORNL of round-robin LBL test samples, which included representative sublots of depleted uranium-bearing TRISO particles fabricated in a production-scale coater by the Chinese Institute of

Nuclear and New Energy Technology (INET) and an LBL benchmarking sample series fabricated by ORNL, which included simulated coating defects and known quantities of an impurity standard.

- Ship AGR-3/4 Compacts 4-3 and 10-1 from INL to ORNL for radial deconsolidation and LBL.
- Ship four compacts from Capsule 2 of the AGR-5/6/7 test train from INL to ORNL for PIE and safety testing.

3.2 High-temperature Materials

- Continue balloting process through the ASME BPVC on life extensions for 316H/304H steels.
- Run additional crack propagation practice tests to compare with previous studies.
- Investigate gas chromatograph and verify functionality of environment testing capabilities.
- Sustain ongoing creep-rupture tests of Alloy 617 specimens containing various geometric discontinuities. The data will be analyzed as tests finish. Metallography and optical microscopy will be used to characterize specimens of interest.
- Analyze the data from an intermediate creep-rupture test (900°C, 28 MPa) of a small-radius base-metal Bridgeman-notch specimen that finished. Update the Larson-Miller Plot with Alloy 617 notch data to include this test.
- Characterize the unruptured notch of the small-radius base-metal Bridgeman-notch specimen that was creep-rupture tested to failure at 900°C and 28 MPa. This will necessitate preparing the specimen using standard metallographic procedures.
- Reload and restart the interrupted creep-rupture test (800°C, 60 MPa) of a base-metal V-notch specimen. The expected life is 8,000 hours. The test was interrupted after 2,000 hours of testing.
- Analyze XCT data from the creep-fatigue test (850°C, $\varepsilon = 0.3\%$, 30 min hold) of a cross-weld specimen with Alloy 617 base and filler metal. The weld was centered with respect to the extensometer and reduced section. The termination criteria for this test was met after three cycles.
- Analyze the SB-SMT test data from the Alloy 617 specimen tested at 950°C with a virtual strain of 0.7% and a 10-minute hold. The test ran for 704 cycles.
- Conduct SMT testing of Alloy 617 at 950°C, 0.2% strain range.
- Weld Alloy 800H with UTP A 2133 Mn, a matching filler metal, using automated gas tungsten arc welding. The weld operator(s), procedure, and performance will be qualified. An INL weld specification will be developed.
- Examine the creep shutdown and restart procedure to ensure reliable testing.
- Begin work on surveillance specimen testing.

3.3 Graphite Development and Qualification

- Begin measurements on AGC-4 samples at Carbon Characterization Lab in October 2021.
- Attend ASME BPVC Week virtual conference (CrowdCompass platform), October 31 – November 5, 2021.
- Participate in ASTM D02.F0 Manufactured Carbon and Graphite Products committee (virtual) meetings November 29 & 30, 2021.

3.4 Methods

- Follow-up on HTTF benchmark meeting action items. Continue working on the benchmark specifications.
- Continue maintenance and repair work on NSTF.
- Wait for comments on the NURETH paper “Sensitivity Analysis and RELAP5-3d Simulation of PCC Phenomena at the High Temperature Test Facility”.

4 REFERENCES

4.1 Fuels Development

4.1.1 AGR-3/4 Radial Deconsolidation

Demkowicz, Paul A., John D. Hunn, Robert N. Morris, Isabella van Rooyen, Tyler J. Gerczak, Jason M. Harp, and Scott A. Ploger. 2015. AGR-1 Post-Irradiation Examination Final Report. INL/EXT-15-36407, Revision 0 Idaho Falls: Idaho National Laboratory.

Helmreich, Grant W., John D. Hunn, Fred C. Montgomery, and Darren J. Skitt. 2021. Radial Deconsolidation and Leach-Burn-Leach of AGR-3/4 Compacts 8-4 and 7-4. ORNL/TM-2021/2178, Revision 0. Oak Ridge: Oak Ridge National Laboratory.

Hunn, John D., Richard A. Lowden, James H. Miller, Brian C. Jolly, Michael P. Trammell, Andrew K. Kercher, Fred C. Montgomery, and Chinthaka M. Silva. 2012. “Fabrication and Characterization of Driver-Fuel Particles, Designed-to-Fail Particles, and Fuel Compacts for the US AGR-3/4 Irradiation Test.” Proceedings of the 6th International Topical Meeting on High Temperature Reactor Technology (HTR-2012). Tokyo, October 28–November 1, 2012. Also published in Nuclear Engineering and Design 271: 123–130.

Hunn, John D., Robert N. Morris, Charles A. Baldwin, Fred C. Montgomery, Chinthaka M. Silva, and Tyler J. Gerczak. 2013. AGR-1 Irradiated Compact 4-4-2 PIE Report: Evaluation of As-Irradiated Fuel Performance with Leach Burn Leach, IMGA, Materialography, and X-ray Tomography. ORNL/TM-2013/236, Revision 0. Oak Ridge: Oak Ridge National Laboratory.

Hunn, John D., and Fred C. Montgomery. 2020. Data Acquisition Method: Leach-Burn-Leach Analysis of Irradiated Fuel Compacts Using a Soxhlet Extractor in the 3525 Hot Cell. AGR-CHAR-DAM-37, Revision 4. Oak Ridge: Oak Ridge National Laboratory.

Stempien, John D., Paul A. Demkowicz, Jason M. Harp, and Philip L. Winston. 2018. AGR-3/4 Experiment Preliminary Mass Balance. INL/EXT-18-46049, Revision 0. Idaho Falls: Idaho National Laboratory.

Stempien, John D., John D. Hunn, Robert N. Morris, and Paul A. Demkowicz. 2021. AGR-2 TRISO Fuel Post-Irradiation Examination Final Report. INL/EXT-21-64279, Revision 0. Idaho Falls: Idaho National Laboratory.

4.1.2 FITT Oxidation Studies

Cao, Fangcheng, De Zhang, Qingjie Chen, Hao Li, and Hongqing Wang. 2020. “Evaluation of Oxidation Performance of TRISO Fuel Particles for Postulated Air-Ingress Accident of HTGR.” Journal of Chemistry 2020: 6568987. doi:10.1155/2020/6568987.

Costello, John A., and Richard E. Tressler. 1986. “Oxidation Kinetics of Silicon Carbide Crystals and Ceramics: I, in Dry Oxygen.” Journal of the American Ceramics Society 69 (9): 674–681.

Gerczak, Tyler J., John D. Hunn, Robert N. Morris, Fred C. Montgomery, Darren J. Skitt, Charles A. Baldwin, John A. Dyer, Brian D. Eckhart. 2020. "Analysis of fission product distribution and composition in the TRISO layers of AGR-2 fuel." Nuclear Engineering and Design 364: 110656.

Gerczak, Tyler J., Zachary M. Burns, Darren J. Skitt, Robert N. Morris, and John D. Hunn. 2020. AGR-2 Loose Particle Heating Tests in the Furnace for Irradiated TRISO Testing. ORNL/TM-2020/1715, Revision 0. Oak Ridge: Oak Ridge National Laboratory.

Hawkes, Grant L. 2014. AGR-2 Daily As-Run Thermal Analyses. INL/ECAR-2476, Revision 1. Idaho Falls: Idaho National Laboratory.

Hunn, John D., Fred C. Montgomery, and Peter J. Pappano. 2010. Data Compilation for AGR-2 UCO Variant Compact Lot LEU09-OP2-Z, ORNL/TM-2010/017, Revision 1. Oak Ridge: Oak Ridge National Laboratory.

International Atomic Energy Agency. 1997. Fuel performance and fission product behaviour in gas cooled reactors. IAEA-TECDOC-978. Vienna: International Atomic Energy Agency.

Liu, Rongzheng, Bing Liu, Kaihong Zhang, Malin Liu, Youlin Shao, Chunhe Tang, 2014. "High temperature oxidation behavior of SiC coating in TRISO coated particles." Journal of Nuclear Materials 453: 107–114.

Moormann, Rainer. 2011. "Phenomenology of Graphite Burning in Massive Air Ingress Accidents." Science and Technology of Nuclear Installations: 589747. doi:10.1155/2011/589747.

Narushima, T., T. Goto, T. Hirai, and Y. Iguchi. 1997. "High-Temperature Oxidation of Silicon Carbide and Silicon Nitride." Materials Transactions, JIM 38 (10): 821–835.

Skitt, Darren J., Rachel L. Seibert, Tyler J. Gerczak, John D. Hunn, Zachary M. Burns, and Grant W. Helmreich. 2021. Oxidation testing and examination of AGR-2 TRISO particles. ORNL/TM-2021/2092, Revision 0. Oak Ridge: Oak Ridge National Laboratory.

Sterbentz, James W. 2014. JMOCUP as-run daily depletion calculation for the AGR-2 experiment in ATR B-12 position. INL/ECAR-2066, Revision 2. Idaho Falls: Idaho National Laboratory.

4.2 High Temperature Materials

McMurtrey, Michael and Richard Wright. 2021. "Recommendation for Limiting Conditions for ASME BPVC Section III Division 5 Allowable Stress Criteria." INL/EXT-21-63802, Idaho National Laboratory.

Rupp, Ryann. 2021. "Assessment of Overmatched Filler (Alloy 617) to Improve Alloy 800H Stress Rupture Factors." INL-EXT-21-63328, Idaho National Laboratory.

Wang, Yanli, Mark C. Messner, Robert Jetter, and Ting-Leung Sham. 2019. "Development of Simplified Model Test Method for Creep-Fatigue Evaluation." Proceedings of the ASME 2019 Pressure Vessels and Piping Conference, San Antonio, Texas, USA, PVP2019-93648.